

EFFECTS OF FUSION MASS DENSITY AND FUSION LOCATION ON THE
STRENGTH OF A LUMBAR INTERBODY FUSION

A Thesis

Submitted to the Graduate School
of the University of Notre Dame
in Partial Fulfillment of the Requirements
for the Degree of

Master of Science in Mechanical Engineering

by

Cassi Elizabeth Shelly, B.A.

Glen L. Niebur, Director

Graduate Program in Mechanical Engineering

Notre Dame, Indiana

May 2004

EFFECTS OF FUSION MASS DENSITY AND FUSION LOCATION ON THE
STRENGTH OF A LUMBAR INTERBODY FUSION

Abstract

by

Cassi Elizabeth Shelly

The location and elastic modulus of a fusion mass are important factors for clinical assessment of the adequacy of interbody fusion. Various finite element models of the L3-L4 motion segment were built using the geometry from cross-sectional CT images of the lumbar spine. By applying a compressive load to the superior endplate of the superior vertebral body, the cumulative reaction force and maximum principal strain value could be computed. Using these values and the compressive failure strain for vertebral cancellous bone, the maximum sustainable load before failure could be computed. It was consistently noted that as the density of the fusion increased, the maximum load increased. Furthermore, when the density of the fusion mass became equal to or greater than the vertebral bodies, failure was seen in the vertebral body whereas for lesser densities failure was seen in the fusion. As the fusion was laterally displaced, failure load decreased, and as the fusion was posteriorly displaced, the failure load increased. In conclusion, the results validated the importance of clinical assessment of both fusion density and fusion location.

CONTENTS

FIGURES	iv
TABLES	vii
ACKNOWLEDGMENTS	viii
CHAPTER 1: INTRODUCTION	
1.1 Fundamental Spinal Anatomy.....	1
1.2 Spinal Disorders.....	4
1.3 Literature Review.....	8
CHAPTER 2: PRELIMINARY MODELS	
2.1 Initial Model of Fused Lumbar Motion Segment	13
2.1.1 Methods.....	13
2.1.2 Material Properties.....	15
2.1.3 Loading Conditions and Constraints.....	17
2.1.4 Results.....	17
2.1.5 Discussion.....	19
2.2 Enhanced Preliminary Model	21
2.2.1 Methods.....	22
2.2.2 Material Properties.....	24
2.2.3 Loading Conditions and Constraints.....	25
2.2.4 Results.....	25
2.2.5 Discussion.....	26
2.3 Conclusions.....	27
CHAPTER 3: VALIDATION OF KEY METHODS AND RESULTS	
3.1 Introduction.....	29
3.2 Method to Compute Failure Load.....	29
3.3 Convergence Study	37
3.4 Conclusions.....	39
CHAPTER 4: EFFECTS OF FUSION LOCATION AND FUSION DENSITY	
4.1 Introduction.....	41
4.2 Methods.....	43
4.3 Material Properties.....	45
4.4 Loading Conditions and Constraints.....	46
4.5 Results.....	47

4.6 Discussion	48
CHAPTER 5: EFFECTS OF FACET JOINT CONTACT	
5.1 Modeling Facet Joint Contact	54
5.2 Methods.....	54
5.3 Results.....	56
5.4 Discussion.....	59
CHAPTER 6: CONCLUSIONS	
6.1 Goal of this Study	61
6.2 Summary	61
6.3 Future Work.....	62
6.4 Conclusions.....	64
APPENDIX	
A1: Procedure for Creating Triangulated Surface Mesh	66
A2: Procedure for Creating a Finite Element Mesh.....	70
WORKS CITED	72

FIGURES

Figure 1.1: Diagram of cervical, thoracic, lumbar, and sacrum regions of the Spine	2
Figure 1.2: Diagram of the vertebral structures	3
Figure 1.3: Patient with multiple fused vertebrae	5
Figure 1.4: CT image showing an osteophyte that developed off of a vertebral body	5
Figure 1.5: Fusion using a titanium mesh cage.....	7
Figure 1.6: Femoral ring allograft with cancellous plug.....	7
Figure 2.1: CT scan of cross-sectional slice through lumbar vertebral body	14
Figure 2.2: Finite element mesh of fused lumbar motion segment.....	15
Figure 2.3: Relationship between apparent density (g/cc) and Young's Modulus (MPa).....	16
Figure 2.4: Strain Distribution Across Fusion Mass (mm/mm)	19
Figure 2.5: Lateral displacement of fusion mass versus maximum axial load sustainable by LIF for constant fusion density of 0.25 g/cc	20
Figure 2.6: Fusion mass density versus maximum axial load sustainable by LIF for a 0 mm lateral displacement of the LIF.....	20
Figure 2.7: Finite element mesh of fused lumbar motion segment including posterior elements	23
Figure 3.1: Failure load for all fusion locations and a fusion mass density of 0.15 g/cc using the maximum strain and an average of the highest 1% and 5% strain values of the fusion elements.....	31
Figure 3.2: Failure load for all fusion locations and a fusion mass density of 0.20 g/cc using the maximum strain and an average of the highest 1% and 5% strain values of the fusion elements.....	31

Figure 3.3: Failure load for all fusion locations and a fusion mass density of 0.25 g/cc using the maximum strain and an average of 1% and 5% of fusion and vertebral body elements	33
Figure 3.4: Failure load for all fusion locations and a fusion mass density of 0.30 g/cc using the maximum strain and an average of 1% and 5% of fusion and vertebral body elements	33
Figure 3.5: Failure load for all fusion densities for a central-posterior fusion location using the maximum strain and an average of 1% and 5% of fusion and vertebral body elements	34
Figure 3.6: Failure load for all fusion densities for a central-central fusion location using the maximum strain and an average of 1% and 5% of fusion and vertebral body elements	35
Figure 3.7: Failure load for all fusion densities for a lateral-posterior fusion location using the maximum strain and an average of 1% and 5% of fusion and vertebral body elements	35
Figure 3.8: Failure load for all fusion densities for a lateral-central fusion location using the maximum strain and an average of 1% and 5% of fusion and vertebral body elements	36
Figure 3.9: Failure load for all fusion densities for a lateral-anterior fusion location using the maximum strain and an average of 1% and 5% of fusion and vertebral body elements	36
Figure 3.10: Failure load for all fusion densities for a central-anterior fusion location using the maximum strain and an average of 1% and 5% of fusion and vertebral body elements	37
Figure 4.1: The six fusion placements investigated under compressive loading.....	43
Figure 4.2: Finite element mesh of fused lumbar motion segment with fusion mass located centrally	45
Figure 4.3: The maximum sustainable load (N) plotted for each fusion location as a function of fusion mass density (g/cc).....	48
Figure 4.4: Contour plots of fusion mass for each location at a density of 0.15 g/cc showing strain distribution	49
Figure 4.5: Contour plots of fused motion segment for a central-posterior location at a density of 0.30 g/cc showing strain distribution	50

Figure 5.1: The maximum sustainable load (N) plotted for each fusion location as a function of fusion mass density (g/cc).....	56
Figure 5.2: A comparison between the maximum sustainable load (N) with and without contact for a fusion mass density of 0.15 g/cc for each fusion location.....	57
Figure 5.3: A comparison between the maximum sustainable load (N) with and without contact for a fusion mass density of 0.20 g/cc for each fusion location.....	57
Figure 5.4: A comparison between the maximum sustainable load (N) with and without contact for a fusion mass density of 0.25 g/cc for each fusion location.....	58
Figure 5.5: A comparison between the maximum sustainable load (N) with and without contact for a fusion mass density of 0.30 g/cc for each fusion location.....	58

TABLES

TABLE 2.1: MAXIMUM AXIAL LOAD SUSTAINABLE BY LIF	18
TABLE 2.2: FAILURE LOADS FOR GIVEN FUSION MASS DENSITY	25
TABLE 3.1: SUMMARY OF CONVERGENCE STUDY RESULTS	39

ACKNOWLEDGMENTS

I would like to thank Medtronic Sofamor Danek for the funding they provided for this research. I would further like to acknowledge Dr. David Polly for his support.

Finally, I would like to thank my advisor, Dr. Glen Niebur, for his direction and ideas.

CHAPTER 1

INTRODUCTION

1.1 Fundamental Spinal Anatomy

The human spine, including 29 vertebrae, the skull, and the pelvis is responsible for a variety of functions such as protection of the spinal cord, nerve roots, and the internal organs of the thorax and abdomen, providing flexibility and motion, and providing structural support and balance in an upright position.

The spine is divided into four regions: the cervical spine, the thoracic spine, the lumbar spine, and the sacrum. The cervical spine is made up of the first seven vertebrae that primarily support the skull and follow a lordotic curve, having a concavity towards the back. There are twelve thoracic vertebrae that follow a kyphotic curve, having a concavity towards the front of the body, in order to make room for the vital organs such as the heart and lungs. Thoracic vertebrae are further distinguished by having ribs. The lumbar region consists of five vertebrae responsible for bearing the weight of the head, neck, shoulders, and thorax and has a lordotic curve. Lastly, five fused kyphotic vertebrae make up the sacrum. The sacrum projects posteriorly in order to make room for such organs as the bladder, reproductive system, and the rectum (Fig. 1.1).

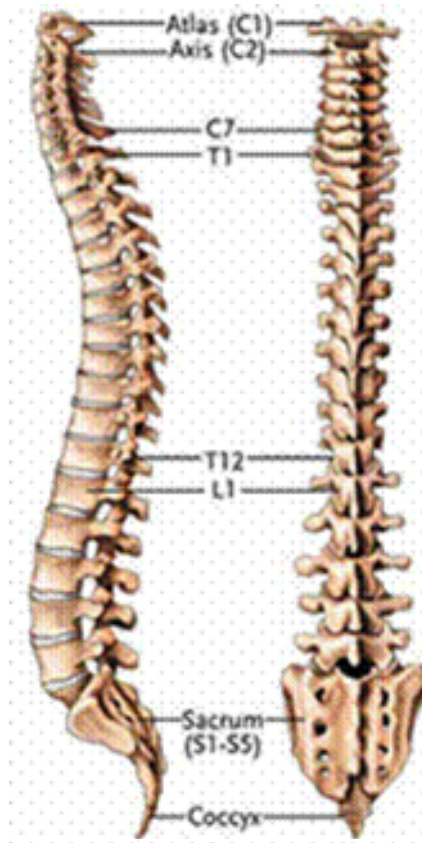


Figure 1.1: Diagram of cervical, thoracic, lumbar, and sacrum regions of the spine

The vertebrae are the bony structures of the spine (Fig. 1.2a). The vertebral body consists of a cancellous core surrounded by a thin dense cortical shell. The pedicles are two dense cortical bone processes that extend posteriorly off of the vertebral body. There are three main spinal processes that serve primarily as insertion points for ligaments and tendons: the articular processes, the transverse processes, and the spinous process. The laminae are flattened plate like structures that extend medially from the pedicles to form the posterior wall of the vertebral foramen. The vertebral foramen, also known as the neural arch, is the region through which the spinal cord and nerve roots pass. Each vertebral body in the cervical, thoracic, and lumbar regions have a pair of facet joints. These joints are located on the posterior

side of the vertebral body; the facets from the lower and upper vertebrae join together to form the joint helping to enable spinal movement. The facet joints along with the intervertebral disc function together at each level to form a motion segment, allowing for multiple degrees of motion (Fig. 1.2b).

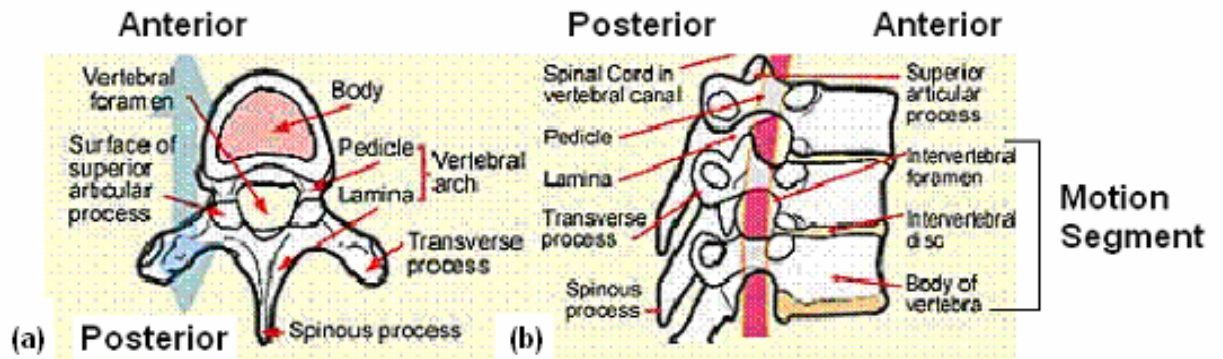


Figure 1.2: Diagram of the vertebral structures

The vertebral bodies are separated by the intervertebral disc. The intervertebral discs are fibro-cartilaginous joints which allow for multiplanar motion permitting flexion, extension, lateral flexion, rotation, and circumduction. The disc consists of an outer area called the annulus fibrosus which is primarily made up of collagen fibers. The nucleus pulposus makes up the inner region of the disc and is much more gelatinous than the annulus fibrosus. In younger adults, the nucleus can be up to 85% water. However, the water content can decrease to as little as 25% in older people. The primary function of the nucleus is to resist compressive loading and act as a shock absorber.

1.2 Spinal Disorders

There are many disorders that affect the spine and require surgical remedies. Direct medical costs for spinal disorders exceed \$20 billion annually (Nachemson 1992).

Scoliosis is defined as an abnormal lateral curvature of the spine and, when severe, can cause lung and heart damage, bone loss, chronic back pain, and even emotional stress (Mayoclinic website). For growing children, a corrective brace can be worn as a non-surgical treatment option. For curves greater than 40 degrees, most doctors recommend surgical treatment, specifically spinal fusion in which various motion segments are immobilized using a bone graft between the vertebral bodies along with stabilizing hardware such as rods, hooks, and screws. Scoliosis can require the fusion of up to ten vertebrae (Fig. 1.3). Kyphosis, similar to scoliosis, is a posterior curve in the sagittal plane that often occurs with aging and can also require the fusion of multiple motion segments.

There are also many degenerative diseases that affect the spine causing changes in the intervertebral disc, the vertebral body, the facet joints, and the ligaments. Degenerative disc disease is a gradual loss of the mechanical competence of the disc. The disc shrinks due to loss of water, the disc space becomes more narrow, sclerosis of the endplate develops resulting in limited diffusion of nutrients to the disc, and osteophytes develop which can infringe on neurological structures (Fig. 1.4). Even though degenerative disc disease can be found at any spinal level, it is most commonly found in the lower lumbar region (Heary and Bono 2002).



Figure 1.3: Patient with multiple fused vertebrae.

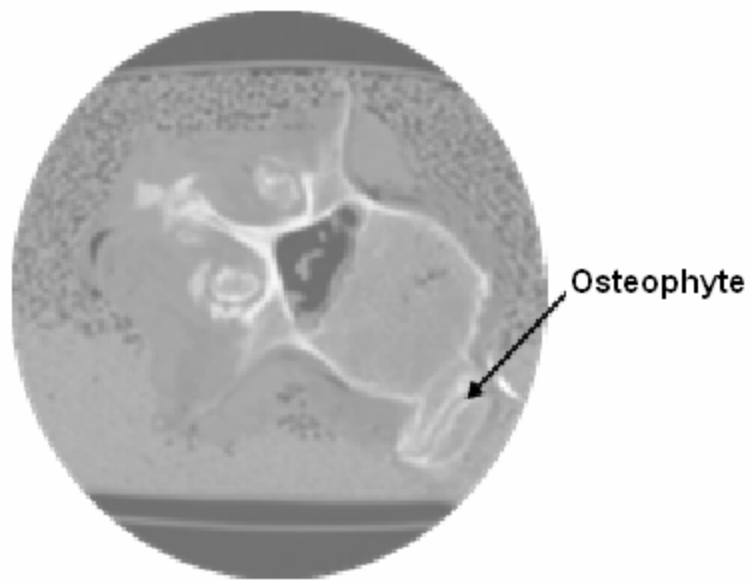


Figure 1.4: CT image showing an osteophyte that developed off of a vertebral body

Spinal fusion is the most common procedure for treatment of degenerative disc disease, with over 250,000 reported procedures performed each year (Pokras and Kubishke 1985). There are two types of fusions: posterolateral fusions and interbody fusions. In a posterolateral fusion, a bone graft is placed in a highly vascularized region located on the transverse processes. In an interbody fusion procedure, the intervertebral disc is removed and replaced with a bone graft usually accompanied by stabilizing hardware. Sometimes the fusion is accompanied by an interbody cage. Typically, this cage is a titanium mesh cylinder that is packed with locally harvested bone and is placed in the disc space (Fig. 1.5) (Heary and Bono 2002). The goal of these implants is to provide mechanical support to the segment or segments being fused, simultaneously taking into account the biology of arthrodesis by allowing the use of autogenous bone to promote fusion (Jost, Cripton et al. 1998). Another fusion technique involves using a femoral ring allograft that is filled with autogenous (retrieved from the same patient) morselized iliac crest graft as a structural support (Fig. 1.6) (Kumar, Kozak et al. 1993).

There are both advantages and disadvantages to these two fusion options. Threaded cages increase stability and decrease displacement rates by providing resistance to device migration (Ray 1997). However, the surface area available for the graft to grow through the cage is not large and this could restrict physiological loading of the bone graft, and thus the ability for the graft to fuse to the vertebral bodies. In a femoral ring allograft, this surface area is often greater (Weiner and Fraser 1998). To increase interbody graft contact with high quality bony bed, greater amounts of

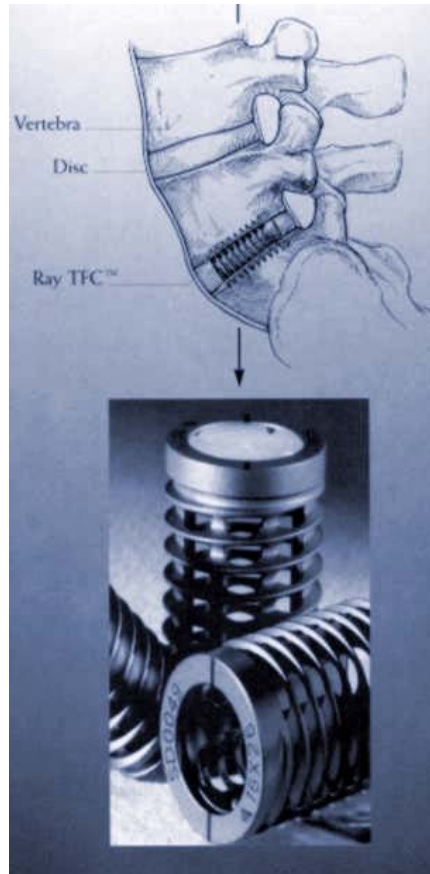


Figure 1.5: Fusion using a titanium mesh cage.

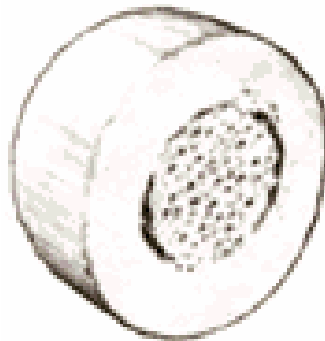


Figure 1.6: Femoral ring allograft with cancellous plug.

subchondral bone need to be removed, increasing the risk of subsidence (Sandhu, Turner et al. 1996).

There are three main surgical approaches to interbody fusions. The posterior lumbar interbody fusion (PLIF) approaches the spine from the back. The anterior lumbar interbody fusion (ALIF) approaches the spine anteriorly. The transforaminal lumbar interbody fusion (TLIF) approaches the spine from the posterior lateral direction in relation to the spine and is considered a minimally invasive posterior approach. The TLIF has recently become a popular choice among surgeons due the benefits it has over the other approaches. These advantages include 1) decreased operative time, 2) decreased blood loss, 3) shorter hospital stays, and 4) decreased cost (Whitecloud, Roesch et al. 2001). Although the TLIF approach has a number of benefits, the access to the intervertebral space during surgery is reduced. This may affect the surgeon's ability to optimally place the fusion mass and thus the success of the fusion. Potential complications associated with interbody fusions also exist. Specifically, fusions can fail if the fusion mass or the underlying vertebral body are not strong enough.

1.3 Literature Review

Computational modeling has become a powerful tool for studying the biomechanics of the lumbar spine over the last decade. Belytschko et al. pioneered this method in the early 1970's. They used this technique to perform a stress analysis of the

intervertebral disc (Belytschko, Kulak et al. 1974). Since then, the finite element method has popularly been applied as a complementary component to experimental investigations (Goel and Gilbertson 1995). Finite element analysis has also been used to predict biomechanical parameters in the lumbar spine such as stresses, strains, and deformation. Kong et al. showed that predicted intradiscal pressures in the L3-L4 disc deviated from in vivo measurements by less than 8.2% (Kong, Goel et al. 1998). Recently, it has been shown that finite element analysis can successfully predict the strength of the vertebra. Crawford et al. showed that highly automated “voxel” finite element models are superior to correlation-based QCT methods in predicting vertebral compressive strength (Crawford, Rosenberg et al. 2003b). Another recent study by Crawford et al. confirmed that this modeling technique provides an excellent noninvasive assessment of vertebral strength (Crawford, Rosenberg et al. 2003b). Liebschner et al. further validated computational finite element studies of the spine based on computed tomography scans. His study showed that using appropriate vertebral shell properties and quantitative CT based modeling of trabecular properties and vertebral geometry, one can accurately predict whole vertebral biomechanical properties (Liebschner, Kopperdahl et al. 2003).

In 1995 Goel et al. built a three-dimensional finite element model of two motion segments in the lumbar spine subjecting it to a uniaxial compressive load (Goel, Ramirez et al. 1995). The remodeling simulations applied to the vertebral body predicted a density distribution within the trabecular bone that was consistent with experimental data. The external shape of the converged model matched the shape of a vertebral body, and the internal remodeling resulted in bone density

distributions that were consistent with previously reported values in the literature. To further understand the form and function of vertebral trabecular bone, Smit et al. used finite element analysis to show that the architecture of the vertebral trabecular bone is related to the mechanical local stress levels (Smit, Odgaard et al. 1997). They concluded that walking is mostly likely the main activity that determines the lumbar vertebral bone architecture.

Finite element analysis, although popular in spine biomechanics, has not been used as extensively to investigate fusion constructs. In 2002, Zander et al. developed a model of a lumbar spinal fusion prior to graft incorporation to investigate the influence of the bone graft size, location, and density on the mechanical behavior of the lumbar spine. This parameter study involved a rectangular shaped graft of varied cross-sectional area, four different fusion locations, and a varied elastic modulus of the bone graft. Graft density affected the stress on the endplate; denser grafts resulted in increased stress. Larger grafts lead to less contact pressure (Zander, Rohlmann et al. 2002b). Zander et al. also used finite element analysis to investigate the differences in mechanical behavior after mono- and bisegmental stabilization. Monosegmental stabilization was studied by modeling a bone graft between the L2 and L3 vertebrae while bisegmental stabilization involved a bone graft between the L2 and L3 and the L3 and L4 vertebrae. There were four graft locations investigated and five different loading scenarios. This model showed that the differences between mono- and bisegmental stabilization are minimal (Zander, Rohlmann et al. 2002a). A recent finite element study by Adam et al. investigated stresses in cage type interbody fusion systems during compressive loading. This study demonstrated that implant

geometry and elastic modulus are both important factors in the mechanical behavior of the fusion and that endplate stresses are highly dependent upon the material properties of the underlying cancellous bone (Adam, Pearcy et al. 2003).

Modeling, usually a complimentary tool to experiment, can actually prove to be more ideal and perhaps more accurate than experimental studies. This technique usually allows for easy parameter manipulation, is non-invasive, and does not require a lengthy time span to obtain results once the models have been built. Often experimental studies are performed in quadrupeds such as horses or rats (DeBowes, Grant et al. 1984) (Kawaguchi, Matsui et al. 1998). Loading and anatomy are quite different in these animals when compared to humans. Therefore, finite element analysis with accurate loading and anatomical geometry may prove to be more precise.

Experimental studies suggest that in order to avoid failure by subsidence, the fusion mass should cover thirty percent of the area of the vertebral body endplate (Closkey, Parsons et al. 1993). This finding was based on subsidence of a cortical bone block into the central region of the vertebral body. Clinically, the bridging of trabeculae is considered to be the “sentinel sign” of a successful fusion. However, this does not consider the quality of the bone within the fusion mass, its size, or placement on the vertebral body. The geometry, location, and the elastic modulus of the fusion mass may also be important factors for clinical assessment of the adequacy of interbody fusion. The overall goal of this research was to investigate the effects of variations in the bone density and fusion mass location in lumbar interbody fusion. Specifically, the aims were to 1) develop a three dimensional finite element model of

a lumbar motion segment, 2) analyze the effect of fusion mass location and density on the maximum load to failure, and 3) relate our findings to clinical application.

The remainder of this thesis is organized as follows: In Chapter 2, preliminary finite element models will be discussed. These models were developed to investigate fusion placement and fusion density and their effects on the overall strength of a lumbar interbody fusion and to gain insight into the methodology of constructing such models. Chapter 3 discusses validation of the methods used, specifically the use of linear versus quadratic elements and the calculation of the maximum sustainable load until failure using a single element. Chapter 4 discusses the effects of fusion placement and fusion density using a more complete model. However, this particular study does not model contact between the facet joints. In Chapter 5, contact is implemented and the results obtained are compared to the previous model in which contact is inactivated. A summary of the results obtained from this investigative research and suggested directions for further research are given in the final chapter.

CHAPTER 2

PRELIMINARY MODELS

2.1 Initial Model of Fused Lumbar Motion Segment

In many spinal fusions, the posterior elements, i.e. the facet joints and spinous processes, are removed. Experimentally, cages and other interbody devices are typically tested without the posterior elements, as this provides a worst-case scenario for the behavior of the device in vivo. Similarly, subsidence of bone grafts has been investigated using vertebral bodies without posterior elements (Closkey, Parsons et al. 1993). Most finite element analyses of whole bones have assumed isotropic material properties dependent on local bone density. This assumption is often reasonable, particularly in the axially loaded spine where stresses and strains are predominantly uniaxial.

The goal of this preliminary model was to investigate the effects of fusion mass size and location on the overall strength of a fused motion segment when no posterior elements were present, and assuming simplified isotropic material properties.

2.1.1 Methods

A cadaveric lumbar spine from a 96 year old male was obtained from the Indiana

University Medical School. Using a GE Prospeed CT scanner, 143 cross-sectional images were obtained (Fig. 2.1).

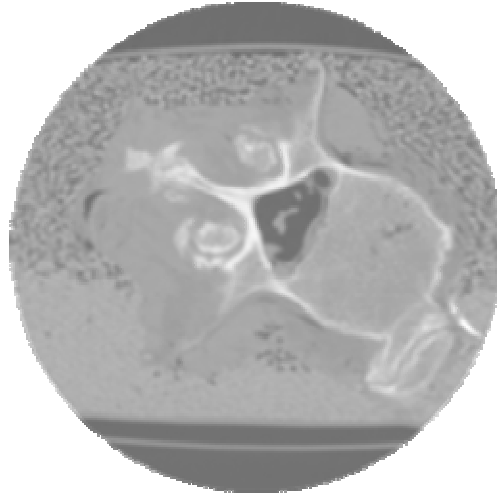


Figure 2.1: CT scan of cross-sectional slice through lumbar vertebral body

The images had an in-plane resolution of 0.26 mm/pixel and were spaced 1.5 mm apart. The data between each slice was interpolated using cubic convolution interpolation (IDL, Research Systems, Inc., Boulder, Colorado) to construct uniform 0.26 mm cubic voxels. The resulting 819 image slices were segmented using NIH Image (National Institutes of Health, Version 1.63) by carefully tracing the spinal geometry using a built in threshold function. The goal was to obtain a model of a motion segment consisting of two vertebral bodies not including posterior elements. The vertebrae were selected based on the absence of fractures or other abnormalities such as osteophytes. The resulting black and white images were stacked to form a three-dimensional volumetric data set. The volume was then smoothed using a 3x3 box filter to avoid the stair-step effect caused by stacking pure black and white images. The smoothed volume was transformed into a triangulated isosurface using

public domain software (polyr, J. J. Jensen) (Appendix A1).

The triangulated surface mesh was converted to STL format and imported into a finite element modeling package (Truegrid, XYZ Scientific Applications, Inc., Livermore, CA) (Appendix A2). Once this surface was imported, it was used as a projection boundary along with a manually created elliptical cylinder that ran through the center of the superior endplate of the superior vertebral body through the center of the inferior endplate of the inferior vertebral body. Using the butterfly projection method, a mesh representing a fused lumbar motion segment was created consisting of 3432 linear brick elements and 4166 nodes (Fig. 2.2).

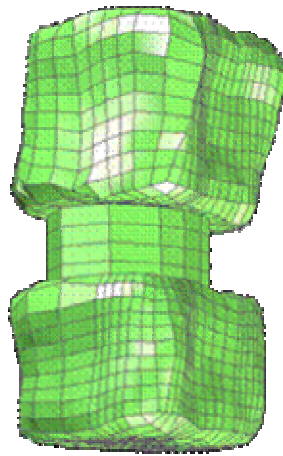


Figure 2.2: Finite element mesh of fused lumbar motion segment

2.1.2 Material Properties

This model assumed isotropic material properties. The vertebral bodies were assigned an apparent density of 0.25 g/cc (Morgan, Bayraktar et al. 2003). Relating bone density to the elastic modulus using the equation, $E=9430*\rho^{1.96}$ (Keaveny, Morgan et al. 2001) (Fig. 2.3), the equivalent modulus was 623.0 MPa.

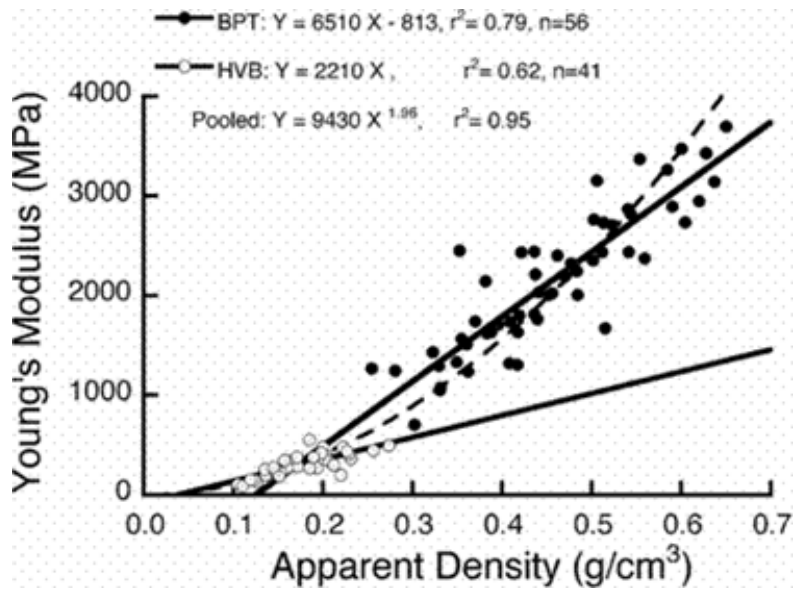


Figure 2.3: Relationship between apparent density (g/cc) and Young's Modulus (MPa) (Keaveny, Morgan et al. 2001)

The fusion mass was assigned three different densities: 0.20 g/cc, 0.25 g/cc, and 0.30 g/cc corresponding to moduli of 402.3 MPa, 623.0 MPa, and 890.6 MPa, respectively. It was rigidly fixed to the vertebral body to simulate a fully incorporated fusion and covered an area greater than 30% of the area of the vertebral body endplate (Closkey, Parsons et al. 1993). Three fusion mass locations were examined to investigate the effect on the strength of the fused motion segment. The fusion mass was located centrally between the two vertebral body endplates and was then displaced laterally 1 mm and 2 mm. Due to the symmetry of the model, the fusion was only laterally displaced in one direction.

2.1.3 Loading Conditions and Constraints

A uniform pressure was applied to the endplate of the superior vertebral body. Boundary conditions were imposed on the inferior vertebral body to constrain movement in all directions. The maximum total load before exceeding the compressive failure strain of vertebral cancellous bone (0.77%) (Morgan, Bayraktar et al. 2003) in either the fusion mass or the vertebral body was computed for each case.

2.1.4 Results

Higher bone densities resulted in greater strength but were limited by the density of the underlying cancellous bone in the vertebral body (Table 2.1). It was observed that when the fusion mass was more dense than the vertebral body, failure occurred in the vertebral body. However, for fusion densities of 0.20 g/cc and 0.25 g/cc, failure occurred in the fusion mass. As the fusion was laterally displaced from the most central placement, the strength of the LIF decreased.

Contour plots of strain showed that the centrally located fusion mass, as expected, had the most uniform strain distribution. As the fusion mass was displaced, the strain distribution became less uniform. The fusion mass experienced higher strains in the direction in which it was displaced and lower strains in the opposite direction (Fig. 2.4).

TABLE 2.1

MAXIMUM AXIAL LOAD SUSTAINABLE BY LIF

Lateral displacement of fusion mass (mm)	Fusion Mass Density (g/cc)		
	0.20	0.25	0.30
	Maximum Axial Load Sustainable by LIF (Newtons)		
0	1162.4	1722.0	2366.5
1	1018.2	1504.5	2063.5
2	888.3	1309.1	1791.7

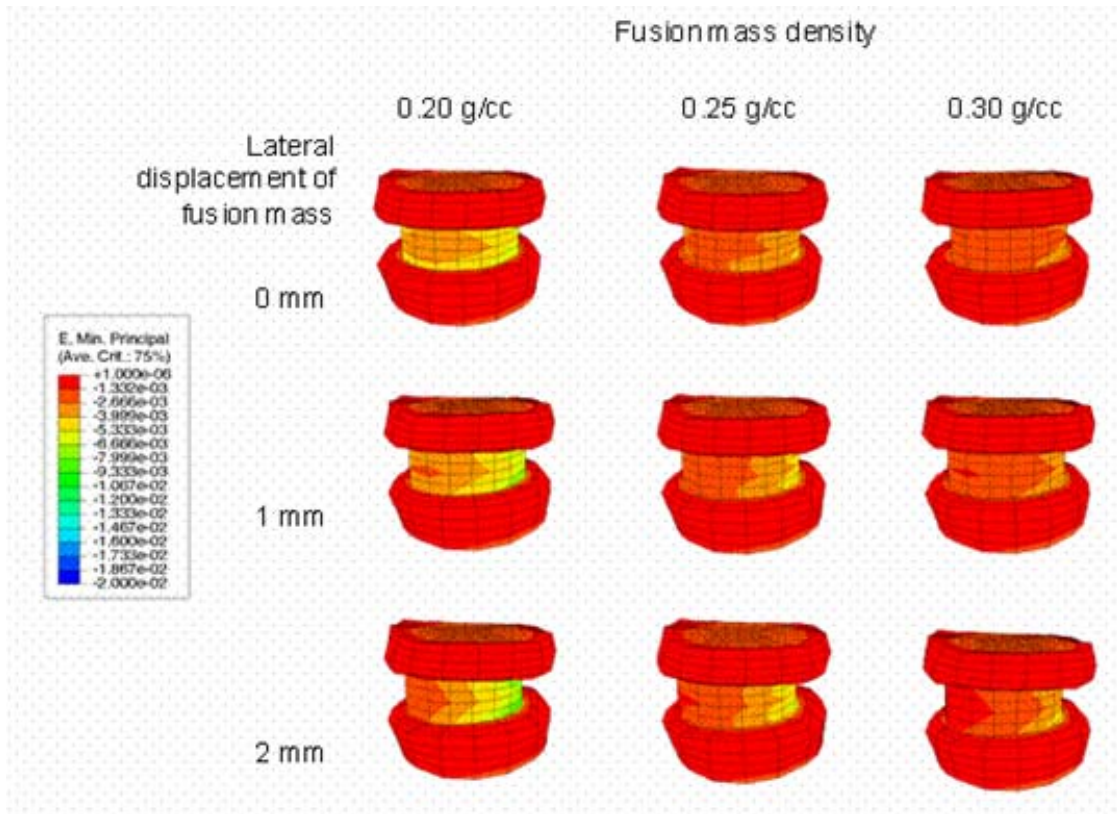


Figure 2.4: Strain Distribution Across Fusion Mass (mm/mm)

2.1.5 Discussion

The goal of this model was to investigate the effects fusion mass density and fusion displacement have on the overall strength of the interbody lumbar fusion while gaining insight into the modeling methodology. Both parameters investigated had a substantial effect on the maximum axial load sustainable by a lumbar interbody fusion. By plotting the maximum axial load versus the lateral displacement for a fusion density of 0.25 g/cc (Fig. 2.5) and plotting the maximum axial load versus the fusion density at a 0 mm displacement (Fig. 2.6), the lateral displacement can be compared to a decrease in bone density.

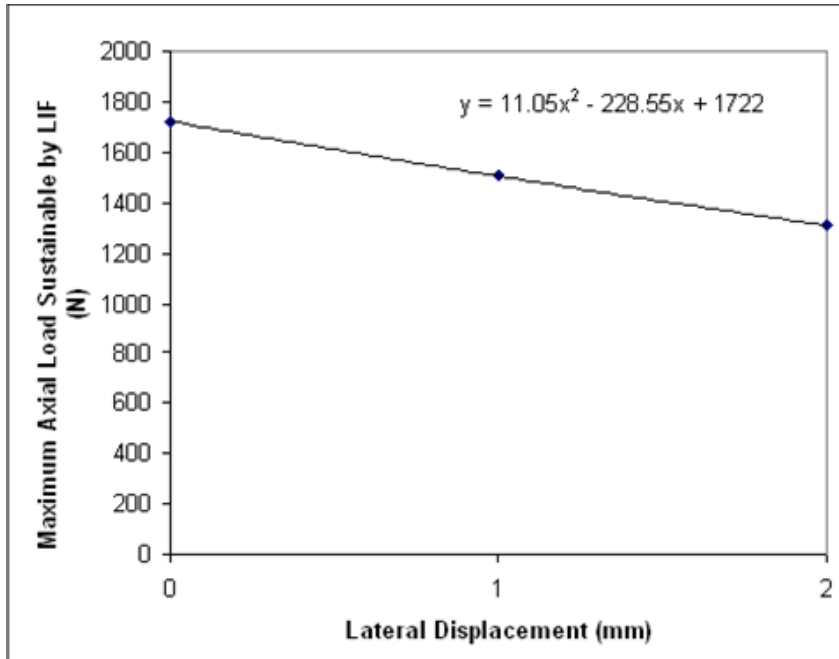


Figure 2.5: Lateral displacement of fusion mass versus maximum axial load sustainable by LIF for constant fusion density of 0.25 g/cc

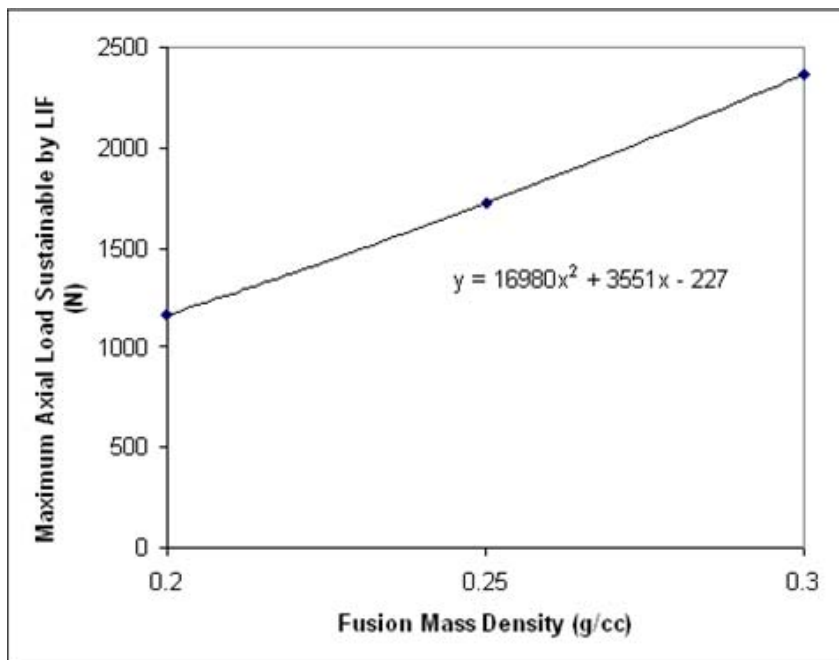


Figure 2.6: Fusion mass density versus maximum axial load sustainable by LIF for a 0 mm lateral displacement of the LIF

For a fusion mass having a density of 0.25 g/cc that is displaced 2 mm, the maximum axial load sustainable was 1309.1 N. The axial load of 1309.1 N can be plotted on Figure 2.6 to show that it would have an equivalent fusion mass density of 0.2138 g/cc. Therefore, a 2 mm lateral displacement of the fusion mass decreased the maximum load comparable to 14.5% decrease in the fusion mass density.

Even though this model does offer insight into the importance of investigating the effects of fusion mass density and placement, a more detailed model can give a more complete understanding of the effect of varying such parameters on the strength of an interbody lumbar fusion. Notably, the incorporation of posterior elements, anisotropic material properties, and a cortical shell may have a substantial effect on the maximum load to failure.

2.2 Enhanced Preliminary Model

In part, the accuracy of these models depend upon the material properties assigned to the trabecular bone. Wolff's law states that trabecular bone responds to mechanical stimuli which leads to the alignment of the trabeculae with the principal stress directions (Wolff 1892). This explains the mechanical anisotropy observed in vertebral cancellous bone. Vertebral cancellous bone is highly anisotropic with a greater strength in the axial direction (Nicholson, Cheng et al. 1997). Experimental studies have shown the elastic modulus in the lateral and anterior-posterior directions is approximately 1.5 times less than the elastic modulus in the axial direction (Ulrich, van Rietbergen et al. 1999).

When investigating the strength of a vertebral body, some finite element models neglect to include the posterior elements. Anatomically, the pedicles have a potential role as a structural buttress, providing support through their attachment to the posterior wall of the vertebral body (Whyne, Hu et al. 1998). Using transversely isotropic trabecular bone properties, the inclusion of the posterior arch results in a substantial decrease in the maximum strain and therefore yielding more accurate predictions for vertebral body strength predictions from finite element models (Whyne, Hu et al. 1998).

In order to expand upon the original model, a full lumbar motion segment was used including posterior elements. Also, more realistic material properties were enforced for the vertebral bodies, modeling them as transversely isotropic. This study continued to investigate the effects of fusion mass density on the strength of a lumbar interbody fusion incorporating different density distributions.

2.2.1 Methods

Similar to the first model, this model was constructed using the original 143 computed tomography scans of the lower lumbar region. However, this model incorporated the posterior elements which were not included on the earlier model. The tracing of the spinal geometry incorporated the pedicles, the superior articular processes, the transverse processes, the inferior articular processes, and the spinous process. Also, a centrally located ellipse was drawn in all the images where the vertebral disk would normally be found. This ellipse translated into a three dimensional elliptical fusion mass connecting the superior and inferior vertebral

bodies. The endplate was roughly approximated as an ellipse, using NIH image, with the area computed with the following equation: $A = a_1 a_2 \pi$ with a_1 and a_2 being the length of the minor and major axes, respectively. Multiplying this number by 0.33 gave an area value for the fusion mass that covered approximately 33% of the area of the vertebral body endplate (Closkey, Parsons et al. 1993). Major and minor axes values for the fusion mass were chosen so that these values were proportional to those values found for the elliptical region of the endplate. After the images were transformed into a three dimensional triangulated surface mesh and converted into an STL file, they were importable into the finite element meshing program (Hypermesh, Altair Engineering, Troy, MI). The surface triangles were converted into triangular shell elements, and the interior space was filled with tetrahedrons. The resulting mesh consisted of 91262 linear elements and 17864 nodes (Fig. 2.7).

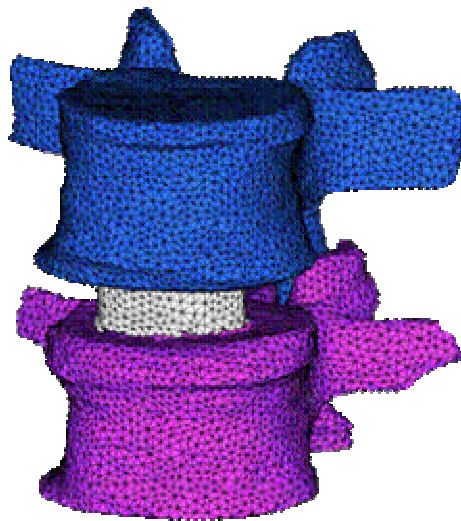


Figure 2.7: Finite element mesh of fused lumbar motion segment including posterior elements

2.2.2 Material Properties

The vertebral body was modeled as transversely isotropic with an apparent density of 0.20 g/cc (Morgan, Bayraktar et al. 2003) and an equivalent elastic modulus of 402 MPa (Liebschner, Kopperdahl et al. 2003) found using the equation, $E=9430*\rho^{1.96}$ (Morgan and Keaveny 2001). The transverse modulus was assumed to be 0.55 times the axial modulus (Ulrich, van Rietbergen et al. 1999). The cortical shell was modeled as 0.35 mm thick (Silva, Wang et al. 1994) with isotropic properties with a modulus of 402 MPa. The shell elements were not intact under the fusion. This was to simulate the decortication of the vertebral body done prior to a lumbar interbody fusion procedure. The posterior elements were also modeled as isotropic with a density of approximately 1.3 g/cc and an elastic modulus of 13 GPa (Silva, Wang et al. 1994). The fusion mass, covering approximately 33% of the area of the vertebral body endplate, was assigned both constant density values as well as density values that varied concentrically. Three constant fusion densities were investigated: 0.25 g/cc, 0.20 g/cc, and 0.15 g/cc which corresponded to the elastic moduli of 623 MPa, 402 MPa, and 229 MPa, respectively. Two models were constructed in which the fusion mass had a varying density. The mass was divided into two sections: a central ellipse consisting of approximately 1/3 the area of the total fusion and an outer elliptical ring consisting of approximately 2/3 the area of the total fusion. The first model assigned the inner elliptical region a density of 0.20 g/cc and the outer ring a density of 0.15 g/cc. The second model assigned the inner region a density of 0.15 g/cc and the outer region a density of 0.20 g/cc.

2.2.3 Loading Conditions and Constraints

A uniform pressure was applied to the endplate of the superior vertebral body, and boundary conditions were imposed on the inferior vertebral body to constrain movement in all directions. The maximum total load before exceeding the compressive failure strain of vertebral cancellous bone, (0.77%) (Morgan, Bayraktar et al. 2003), in either the fusion mass or the vertebral body was computed for each case.

2.2.4 Results

The maximum load to failure was 203 N, 343 N, and 467 N for the 0.15 g/cc, 0.20 g/cc, and 0.25 g/cc fusion mass density, respectively (Table 2.2). When the fusion mass was more dense than the apparent density of the vertebral body, the failure occurred in the vertebral body where as if the fusion mass was equal or less to that of that of the vertebral body, failure occurred in the fusion.

TABLE 2.2
FAILURE LOADS FOR GIVEN FUSION MASS DENSITY

Fusion Mass Density (g/cc)	0.15	0.20	0.25
Maximum Load before Failure (N)	203	343	467

When decreasing the density of the outer rim of the fusion mass to 0.15 g/cc while having an inner region with a density of 0.20 g/cc, the failure load was calculated to be 216 N. Increasing the density of the outer rim to 0.20 g/cc with an inner region density of 0.15 g/cc had a failure load of 328 N.

2.2.5 Discussion

One goal of this model was to continue to form a sound methodology of building a finite element model of a lumbar motion segment with a fusion mass while making the model more complete with anisotropic properties and including posterior elements. Another goal was to continue the investigation of the effects fusion mass density on the overall strength of the lumbar interbody fusion. Similar to the first model, it was found that as the density of the fusion mass was increased, the maximum load sustainable by the LIF also increased. The loads computed in this case, however, were significantly lower than those found in the first model. This is attributed to the fact that the fusion mass was considerably smaller in the model, approximately 33% of the area of the vertebral body endplate (Closkey, Parsons et al. 1993). The loads calculated in this model were similar to those found experimentally when the posterior elements were removed (Closkey, Parsons et al. 1993).

The variations of density within the fusion mass substantially affected the maximum load. By decreasing the density of the outer ring to 0.15 g/cc, the maximum load was only 6% greater than if the entire fusion had a density of 0.15 g/cc. When the outer ring density was 0.20 g/cc and the central region had a decreased density of 0.15 g/cc the failure load was approximately 4% less than that

found with a constant fusion mass density of 0.20 g/cc. These varied densities are important parameters to investigate clinically. A fusion mass with a denser outer ring can be compared to a femoral ring allograft whereas a fusion mass with a denser inner region can be compared to the use of a cage in a LIF procedure.

This enhanced model had many strengths when compared with the initial model. Anisotropic properties, inclusion of the cortical shell, and the inclusion of the posterior elements added to the model's completeness. Even though this model was more advanced, there were limitations. Contact was not modeled between the posterior elements. However, if contact had been modeled, some of the load would have been distributed to the posterior elements and actually increased the strength of the LIF. Thus, the current results represent a worst-case scenario. Clinically, it could be compared to a double facetectomy, which is common when the interbody fusion is performed as a posterior surgery. Another limitation of this model involved the methodology of how the fusion mass was constructed. Finally, the model did not investigate the effects of fusion location which is an important factor in fusion strength.

2.3 Conclusions

These preliminary models served as building blocks for constructing a more complete finite element model of a fused lumbar motion segment. Although the models were limited in detail, they provided important information regarding the role of fusion density on the strength of interbody fusions. The results of this study are summarized as follows:

- As fusion density is increased, the strength of the LIF increases
- As fusion mass is displaced laterally from a central location, the strength of the LIF decreases
- A fusion mass with a denser outer ring and less dense inner core demonstrated a LIF strength almost equivalent to having a fusion mass entirely of the denser substance
- A fusion mass with a less dense outer ring and a more dense inner core demonstrated a LIF strength almost equivalent to having a fusion mass entirely of the less dense substance

CHAPTER 3

VALIDATION OF KEY METHODS AND RESULTS

3.1 Introduction

This chapter examines the method used to compute the load which the lumbar interbody fusion fails. It discusses other options to compute this load and why the method chosen is not only valid but better than the other methods that could have been used. A convergence study examining the effects of using quadratic versus linear elements is also presented in section 3.3 of this chapter.

3.2 Method to Compute Failure Load

The maximum total load before exceeding the compressive failure strain of vertebral cancellous bone, (0.77%) (Morgan and Keaveny 2001), in either the fusion mass or the vertebral body was computed for each case. The Abaqus post-processor was used to output the principal strain in each element as well as the total reaction force. The maximum compressive strain value was used to calculate the failure load by scaling the calculated reaction forces according to the ratio of the failure strain to the maximum strain:

$$F_{Failure} = F_{Reaction} * \frac{\mathcal{E}_{Failure}}{\mathcal{E}_{Max}} \quad (1)$$

where $F_{failure}$ is the maximum sustainable load until failure, $F_{reaction}$ is the total reaction force in the model, $\epsilon_{failure}$ is the compressive failure strain of vertebral cancellous bone (0.0077), and ϵ_{max} is the maximum strain value. The maximum strain value was chosen as the maximum strain value throughout the model given by one single element including both shell and solid elements. This method could produce possible doubt because one element with the maximum strain value out of approximately 145,000 elements could be seen as an outlier and thus diminishing the reliability of our results. It was necessary to perform a study to validate this method and ensure robustness of our results.

For a fusion mass density of 0.15 g/cc and 0.20 g/cc, failure was seen in the fusion mass. A maximum strain value was computed using the highest strain values found in 1% and 5% of the total elements in the fusion and compared to the maximum strain value used to compute the failure load (Figs 3.1 and 3.2).

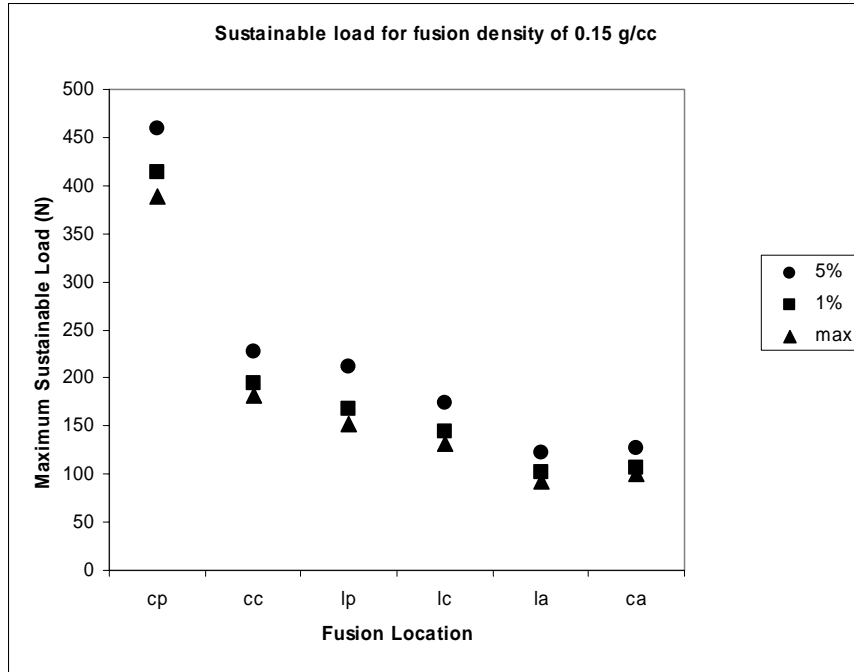


Figure 3.1: Failure load for all fusion locations and a fusion mass density of 0.15 g/cc using the maximum strain and an average of the highest 1% and 5% strain values of the fusion elements.

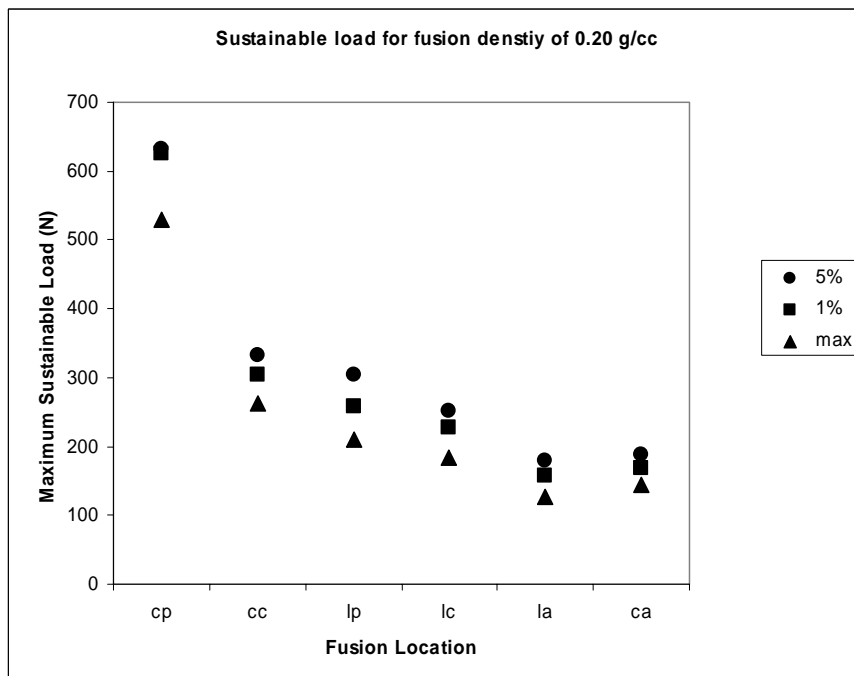


Figure 3.2: Failure load for all fusion locations and a fusion mass density of 0.20 g/cc using the maximum strain and an average of the highest 1% and 5% strain values of the fusion elements.

It is clear that all three methods demonstrate the same trends for a fusion density of 0.15 g/cc and 0.20 g/cc. Even though the maximum loads vary from method to method, this can be expected and won't affect the overall results. The lower the number of elements considered, the lower the sustainable load will be. Therefore, using the maximum value idealizes a worst-case scenario. Furthermore, the numerical values obtained are not as important as the observed trends. The model does not represent an actual patient. Each scenario is different and one would expect different numerical values from case to case. The trends, however, can be used to evaluate different clinical situations because they will remain the same for different cases.

For a fusion density of 0.25 g/cc, the density value was expected to border on failure in the fusion mass versus failure in the vertebral body. It seemed more reasonable to examine the highest strains found in both the vertebral bodies and the fusion mass. Performing a similar study, the differences between the maximum strain value found in the model and the highest strains found in 1% and 5% of the vertebral body and fusion elements combined were examined. The same method was used for a fusion density of 0.30 g/cc. The trends were the same for each case (Figs. 3.3 and 3.4).

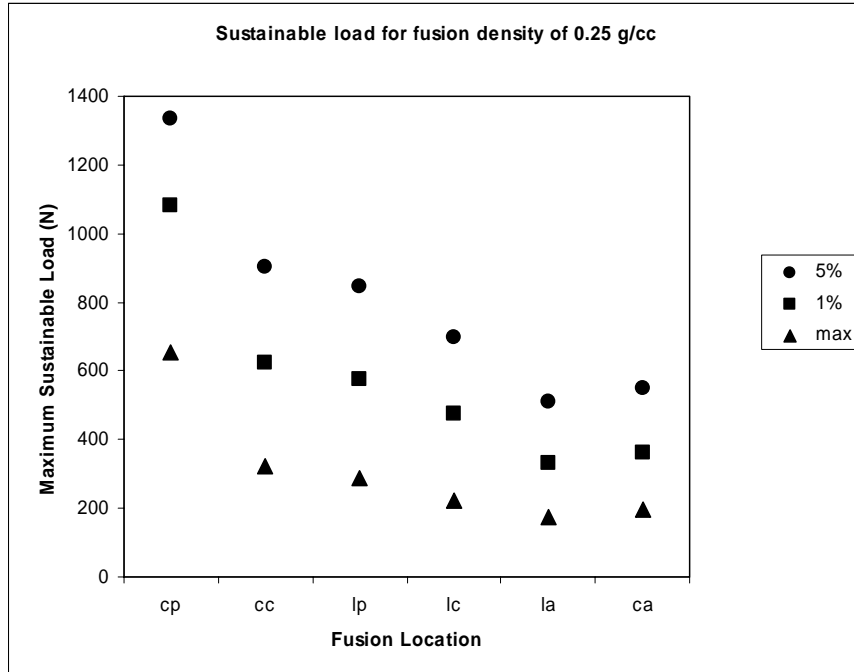


Figure 3.3: Failure load for all fusion locations and a fusion mass density of 0.25 g/cc using the maximum strain and an average of 1% and 5% of fusion and vertebral body elements.

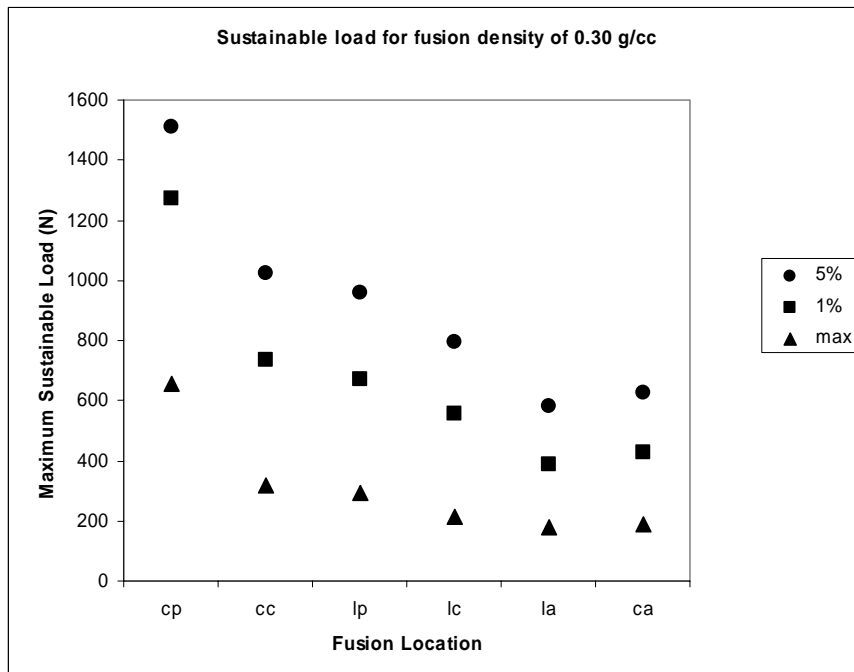


Figure 3.4: Failure load for all fusion locations and a fusion mass density of 0.30 g/cc using the maximum strain and an average of 1% and 5% of fusion and vertebral body elements.

The same trends are noted for all fusion densities and for each method used to obtain the strain value used to calculate the maximum sustainable load.

To further ensure, that using the maximum strain value to compute the load at failure is robust, the sustainable load to failure for individual fusion locations as a function of density was compared (Figs. 3.5-10). In order to compare each density uniformly, it was necessary to compare the maximum load at failure calculated using the maximum fusion density and an average of 1% and 5% of the highest strain values found in both the vertebral body and the fusion mass. Even though for lower densities only fusion elements had been used previously, this was done to ensure consistency.

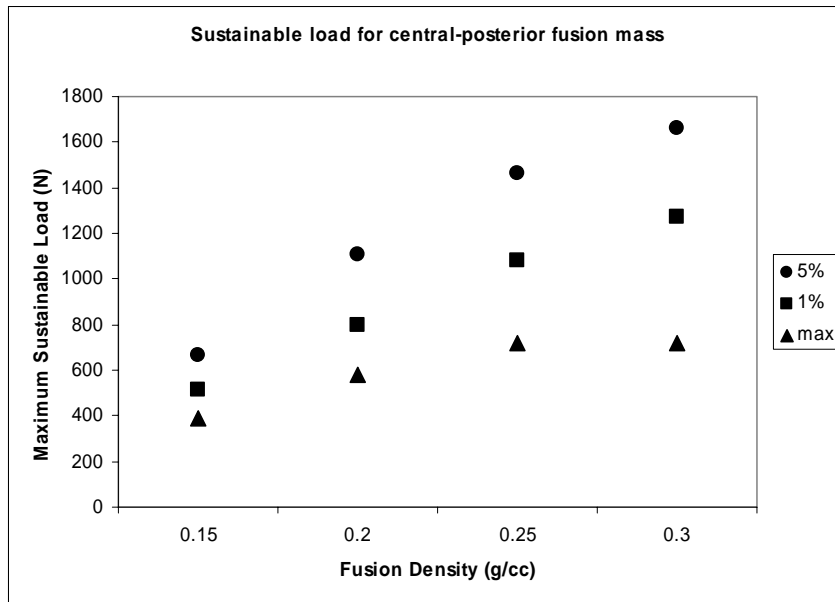


Figure 3.5: Failure load for all fusion densities for a central-posterior fusion location using the maximum strain and an average of 1% and 5% of fusion and vertebral body elements.

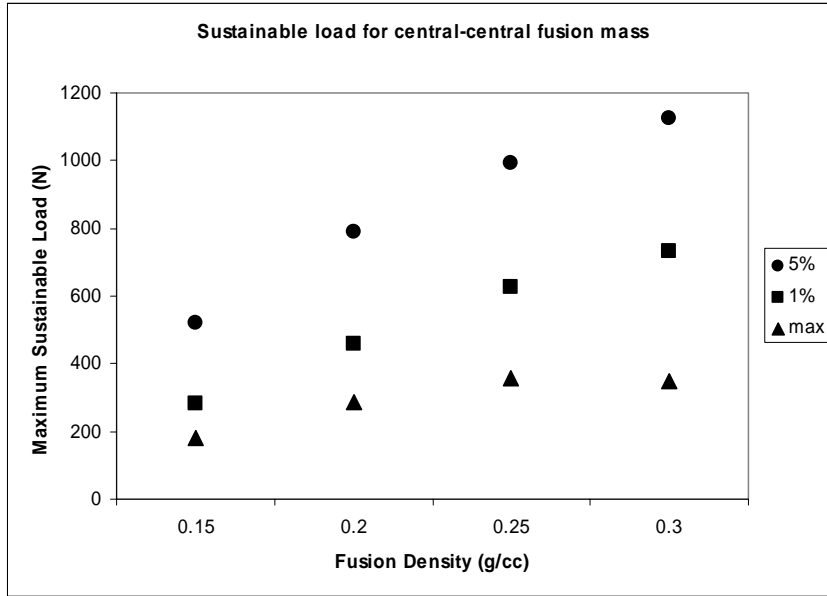


Figure 3.6: Failure load for all fusion densities for a central-central fusion location using the maximum strain and an average of 1% and 5% of fusion and vertebral body elements.

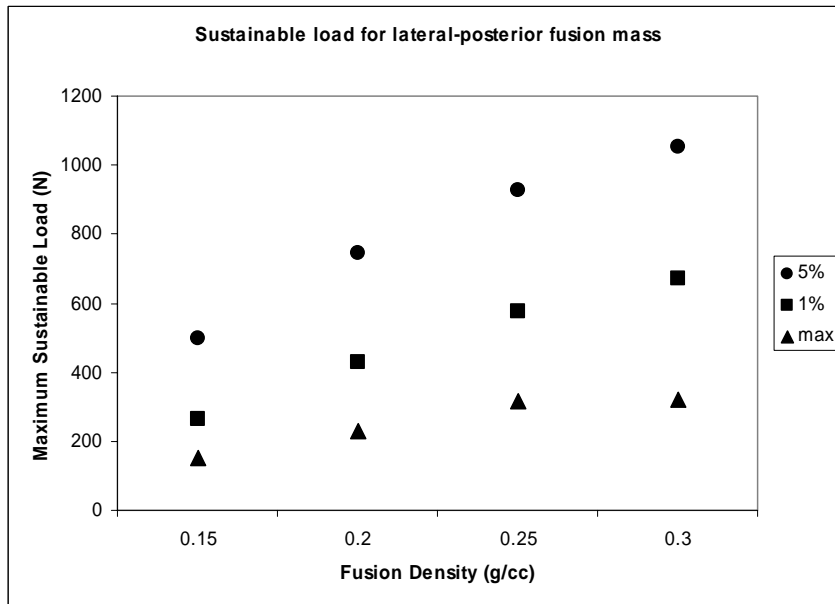


Figure 3.7: Failure load for all fusion densities for a lateral-posterior fusion location using the maximum strain and an average of 1% and 5% of fusion and vertebral body elements.

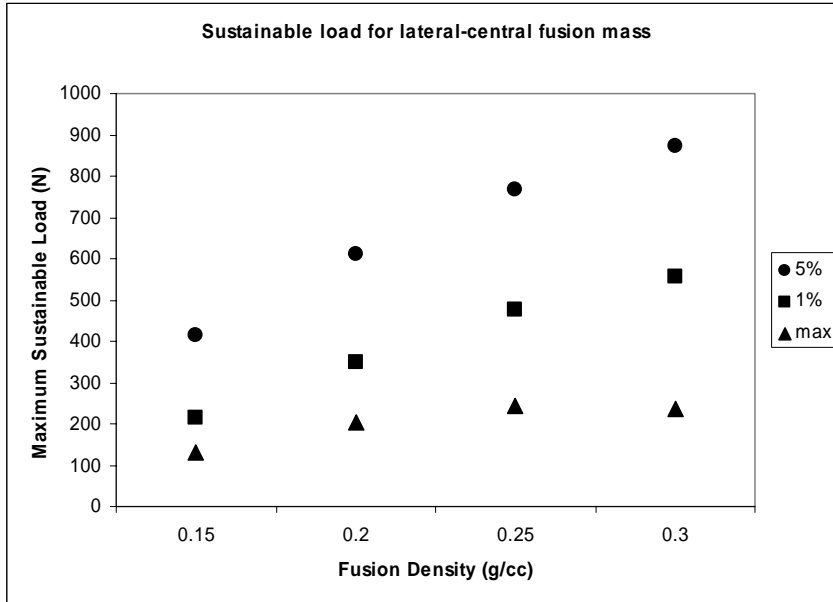


Figure 3.8: Failure load for all fusion densities for a lateral-central fusion location using the maximum strain and an average of 1% and 5% of fusion and vertebral body elements.

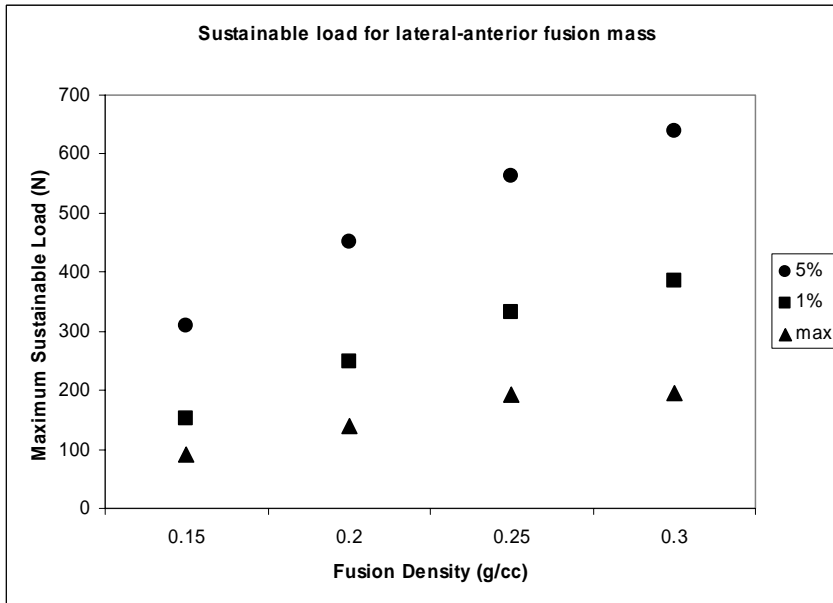


Figure 3.9: Failure load for all fusion densities for a lateral-anterior fusion location using the maximum strain and an average of 1% and 5% of fusion and vertebral body elements.

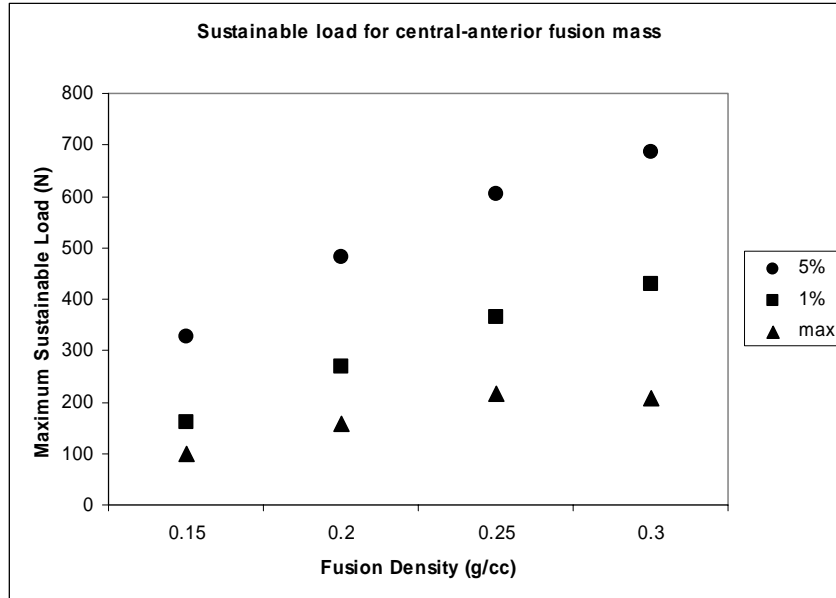


Figure 3.10: Failure load for all fusion densities for a central-anterior fusion location using the maximum strain and an average of 1% and 5% of fusion and vertebral body elements.

The trends for each fusion placement are similar. One difference, however, is that as the density increased in the fusion mass, the maximum sustainable load at failure continued to increase when using 1% and 5% of highest strained elements in the fusion and vertebral body. Looking at the maximum strain value, as the fusion density increases to a density greater than that of the vertebral body, the failure load plateaus and, in some cases, decreases. This is indicative of subsidence and has been shown experimentally (Closkey, Parsons et al. 1993). Also, the differences between the three methods are greater at higher densities.

3.3 Convergence Study

A convergence study was performed to study the effects of using linear versus quadratic elements. A model with quadratic elements should converge to the exact

solution quicker than a model with linear elements. However, this comes with the cost of increased need for memory and increased cpu time. I used three different models to study the convergence. The first model consisted of 91,262 linear elements and 17,864 nodes. The second model consisted of 91,262 quadratic elements and 115,385 nodes. The second model was predicted to more closely approximate the exact solution. A third model was needed to verify the convergence. A model consisting of 135,210 linear elements and 25,145 nodes was chosen. This model should converge at a rate greater than the linear model with less elements and at a lesser rate than the quadratic model. The total strain energy for each model was calculated using the Abaqus post-processor. The first linear model had a total strain energy of 337 N-m. By increasing the number of linear elements, the total strain energy increased to 342 N-m. The total strain energy of the quadratic model was 369 N-m (Table 3.1).

TABLE 3.1
SUMMARY OF CONVERGENCE STUDY RESULTS

	Linear Model 1	Linear Model 2	Quadratic Model
	91,262 elements	135,210 elements	91,262 elements
	17,864 nodes	25,145 nodes	115,385 nodes
Total Strain Energy	337	342	369
Memory Needed (Mb)	515	757	2330
CPU time	370	559	1181

In order to save a memory and CPU time, a linear model was chosen. However, a new model was made consisting of 145,000 linear elements and approximately 28,000 nodes. The above convergence study shows the validity of choosing this linear model.

3.4 Conclusions

The studies discussed in this chapter were important to validate methodologies used to construct the model and to obtain key results. Key points are summarized as follows:

- Similar trends were seen using the maximum strain value and an average of 1% and 5% of the highest strain values to calculate the maximum sustainable load at failure for constant densities and varied fusion placement

- Maximum load at failure increased as density increased for all fusion placements similarly for the three methods used
- When using less elements, the trends were more consistent with experimental studies, i.e. subsidence
- The differences between the methods were greater at higher densities
- The quadratic model had a total strain energy 8.7% greater than the linear model with less elements and 7.3% greater than the linear model with more elements
- The quadratic model required 77.9% more memory and 68.7% more CPU time the linear model with less elements and 67.5% more memory and 52.7% more CPU time than the linear model with more elements
- A linear model with more elements (145,000 elements and 28,000 nodes) than both linear models used in this study was chosen to conserve memory and CPU time

CHAPTER 4

EFFECTS OF FUSION LOCATION AND FUSION DENSITY

4.1 Introduction

Interbody fusions can be surgically approached posteriorly (PLIF), anteriorly (ALIF), and transforaminally (TLIF). The TLIF, a posterior-lateral approach to the spine, has recently gained popularity among spinal surgeons for the benefits it exhibits over the other approaches. These advantages include 1) decreased operative time, 2) decreased blood loss, 3) shorter hospital stays, and 4) decreased cost (Whitecloud, Roesch et al. 2001). Even though this approach exhibits these added benefits, the access to the intervertebral space is greatly reduced. This may reduce the surgeon's ability to optimally place the fusion mass and thus the success of the fusion. Therefore, an investigation of the effect of fusion location on interbody strength is clinically valuable.

Computational modeling has become a tool for studying the biomechanics of the lumbar spine over the last decade. The finite element method has been applied as a complementary component to experimental investigations.(Goel and Gilbertson 1995) Specifically, remodeling simulations applied to the vertebral body have predicted a density distribution within the trabecular bone that was consistent with experimental data.(Goel, Ramirez et al. 1995) Finite element analysis has also been used to predict biomechanical parameters in the lumbar spine such as stresses, strains,

and deformation.(Kong, Goel et al. 1998) It has been shown that the architecture of the vertebral trabecular bone is related to the mechanical local stress levels.(Smit, Odgaard et al. 1997)

Finite element analysis has proved to be a useful technique to model spinal fusion. A model of a lumbar spinal fusion prior to graft incorporation found that graft density affected the stress on the endplate, and the size of the graft influenced the contact pressure.(Zander, Rohlmann et al. 2002b) Another study using this technique demonstrated that implant geometry and elastic modulus are both important factors in the mechanical behavior of the fusion and that endplate stresses are highly dependent upon the material properties of the underlying cancellous bone.(Adam, Pearcy et al. 2003) It has also been shown that the differences in mechanical behavior after mono- and bisegmental stabilization are minimal.(Zander, Rohlmann et al. 2002a) When relating this computational studies to experimental study, experiment suggests that in order to avoid failure by subsidence, the fusion mass should cover thirty percent of the area of the vertebral body endplate.(Closkey, Parsons et al. 1993) This finding was based on subsidence of a cortical bone block into the central region of the vertebral body.

Clinically, the bridging of trabeculae is considered to be the “sentinel sign” of a successful fusion. However, this does not consider the quality of the bone within the fusion mass, its size, or placement on the vertebral body. The geometry, location, and the elastic modulus of the fusion mass may also be important factors for clinical assessment of the adequacy of interbody fusion. This model was developed to continue the investigation of the effects of fusion location and fusion mass density

while enhancing the methodologies of constructing a more complete model. This model, similar to the last model, included the posterior elements and had transversely isotropic material properties. The goal of this study was to investigate different fusion locations that may be more consistent with a TLIF interbody approach. Specifically, six different fusion mass locations were examined with variations in the fusion mass density at each location.

4.2 Methods

The triangulated surface mesh of one L3 and one L4 vertebra were created as described in section 2.2. The triangulated surface mesh, consisting of a L3-L4 motion segment without an intervertebral disc or fusion, was converted to STL format and imported into a finite element modeling package (Hypermesh, Altair Engineering, Troy, MI). Six fusion locations were chosen: central-anterior, central-central, central-posterior, lateral-anterior, lateral-central, and lateral-posterior (Fig. 4.1).

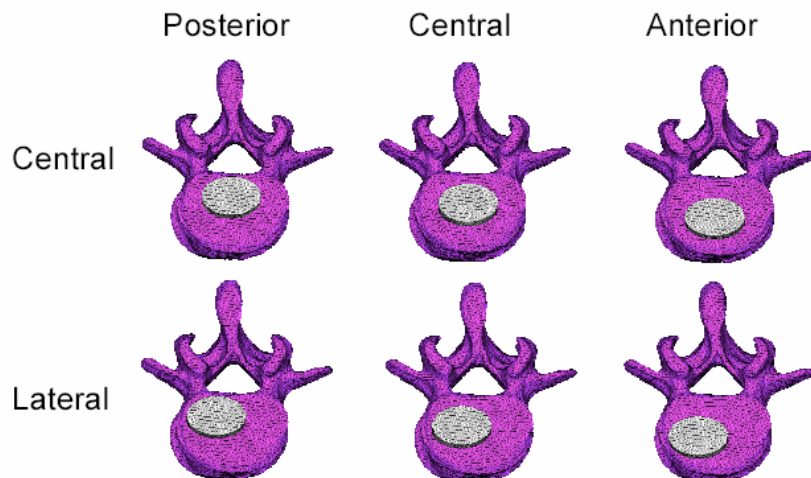


Figure 4.1: The six fusion placements investigated under compressive loading

Due to the symmetry of the vertebral body, the fusion was only modeled as laterally displaced in one direction. Using Hypermesh, an ellipse was constructed with a cross-sectional area approximately 33% of that of the vertebral body endplate. The lengths of the major and minor axes were proportional to the length of the major and minor axes of the vertebral body endplate. First a central-central fusion mass was constructed by aligning the center of the ellipse with the approximate center of the vertebral body. This center was calculated by drawing two imaginary axes across the endplate: one passing through the greatest area possible of the vertebral body transversely and one that ran through the spinous process and the vertebral body from the anterior to posterior sides. This was done for the superior endplate of the inferior vertebral body and for the inferior endplate of the superior vertebral body. The x and y coordinates of the intersection were averaged, and this was the center point used for the fusion mass.

To simulate various surgical placements, the fusion mass was displaced one quarter of the distance from the center point to the edge of the endplate to define the fusion locations of central-posterior, central-anterior, and lateral-central in their respective directions. From the the lateral-central fusion location, the fusion mass was displaced an equivalent amount posteriorly and anteriorly as the central-posterior and central-anterior fusion mass locations to define the lateral-posterior and lateral-anterior fusion locations.

An elliptical shell was constructed connecting the vertebral bodies for each location. The model was then interiorly filled with tetrahedrons, and the fusion shell

was deleted. The resulting mesh consisted of approximately 36,000 shell elements, 110,000 solid elements, and 28,000 nodes (Fig. 4.2).

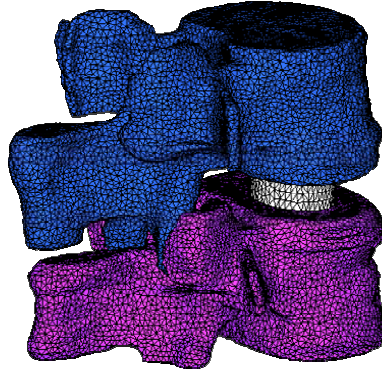


Figure 4.2: Finite element mesh of fused lumbar motion segment with fusion mass located centrally.

4.3 Material Properties

The cancellous core of the vertebral bodies was modeled as transversely isotropic with an apparent density of 0.20 g/cc (Morgan, Bayraktar et al. 2003). Relating bone density to the elastic modulus using the equation, $E = 9430\rho^{1.96}$ (Morgan and Keaveny 2001), the equivalent elastic modulus was 402.3 MPa. The transverse modulus was assumed to be 0.55 times the axial modulus (Ulrich, van Rietbergen et al. 1999). The cortical shell was modeled by shell elements, which were assigned a thickness of 0.35 mm (Silva, Wang et al. 1994) and isotropic properties with a modulus of 608.0 MPa (Liebschner, Kopperdahl et al. 2003). The posterior elements were also modeled as isotropic with a density of approximately 1.3 g/cc and an elastic modulus of 13 GPa (Silva, Wang et al. 1994). The shell elements were left intact under the fusion. Clinically, keeping the endplates intact helps maintain compressive

strength and prevents graft settling (Heary and Bono 2002). The fusion was modeled as isotropic with a density of 0.15 g/cc, 0.20 g/cc, 0.25 g/cc, or 0.30 g/cc. Assuming a similar dependence of modulus to apparent density as for the vertebrae, these densities correspond to moduli of 228.9 MPa, 402.3 MPa, 623.0 MPa and 890.6 MPa, respectively. Isotropic properties were used to model the fusion representative of a graft in which anisotropy had not developed. It was rigidly fixed to the vertebral body to simulate a fully incorporated fusion.

4.4 Loading Conditions and Constraints

A uniform pressure of 1 MPa was applied to the endplate of the superior vertebral body. Boundary conditions were imposed on the endplate of the inferior vertebral body to constrain movement in all directions. The maximum total load before exceeding the compressive failure strain of vertebral cancellous bone (0.77%) (Morgan and Keaveny 2001) in either the fusion mass or the vertebral body was computed for each case (Morgan and Keaveny 2001). The Abaqus post-processor was used to output the maximum compressive principal strain in the vertical direction in each element as well as the total reaction force. The maximum strain value was used to calculate the failure load using the following equation:

$$F_{Failure} = F_{Reaction} * \frac{\epsilon_{Failure}}{\epsilon_{Max}} \quad (1)$$

where $F_{failure}$ is the maximum sustainable load until failure, $F_{reaction}$ is the total reaction force in the model, $\epsilon_{failure}$ is the compressive failure strain of vertebral cancellous bone (0.0077), and ϵ_{max} is the maximum strain value. Because the models are linearly elastic, this relation effectively scales the load to the level that would

result in the minimum principal strain exceeding the failure strain. Studies show that when expressed in terms of strain, failure criteria for a given site may consider the yield point constant for uniaxial monotonic loading (Morgan and Keaveny 2001).

4.5 Results

Higher bone densities resulted in greater strength but were limited by the density of the underlying vertebral cancellous bone (Fig. 4.3). Generally, the highest densities caused failure in the vertebral body, indicative of subsidence while lower densities resulted in failure of the fusion mass. When the fusion mass was assigned a density of 0.25 g/cc, there was failure in the vertebral body for all fusion positions except the lateral-anterior and the lateral-posterior fusion location. However, the maximum strain for the lateral-anterior and lateral-posterior positions was only 4.7% and 4.3% higher in the fusion than in the vertebral body, respectively. For a fusion density of 0.30 g/cc, failure occurred in the vertebral body for all fusion locations.

As the fusion mass was laterally displaced, the sustainable load decreased. Conversely, as the fusion mass was posteriorly displaced, the sustainable load increased (Fig. 4.3). The maximum failure load occurred for a central-posterior placement of the fusion mass at all densities, and was nearly twice as high as the next greatest strength.

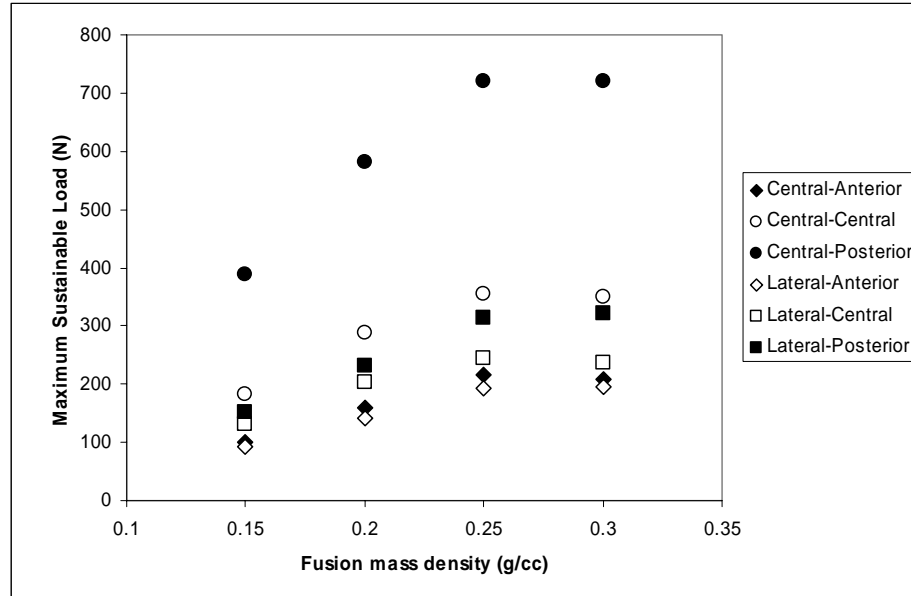


Figure 4.3: The maximum sustainable load (N) plotted for each fusion location as a function of fusion mass density (g/cc).

4.6 Discussion

The goal of this study was to analyze the effect of fusion mass location and density on the strength of an interbody lumbar fusion and relate our findings to clinical application. The results of this study suggest that as the density of the fusion was increased to the point where it was denser than the vertebral body, failure occurred in the vertebral body as opposed to the fusion mass. As the fusion density was increased, the sustainable load increased in a linearly proportional manner until subsidence occurred. At a fusion density of 0.30 g/cc, failure consistently occurred in the vertebral body for all fusion locations, and the maximum load even began to decrease for most cases (Fig. 4.3) This demonstrates the clinical importance of fusion mass density evaluation. If the density of the fusion mass is greater than the density of the vertebral body, there is no advantage compared to the case where the density of the fusion is equal to that of the vertebral body.

The location of the fusion mass had a large affect on the strength. When the fusion mass was located in the central-posterior location, the strain distribution in the fusion mass was much more uniform (Fig. 4.4). This could be attributed to the fact that the fusion mass was more aligned with the center of mass of the motion segment. The uniform distribution of strain allowed for the fusion to carry a higher load. The central-anterior location had a varied strain distribution in which the strain values went from high to low from the posterior to the anterior side of the fusion. Clinically, these results show the importance of fusion placement during anterior and posterior interbody fusions. This suggests that the PLIF or TLIF procedure may be better for ideally placing the fusion mass. Because posterior placement of the fusion mass suggests greater strength, a posterior approach to the spine would allow for easier insertion of a fusion mass in the posterior region as opposed to an anterior approach.

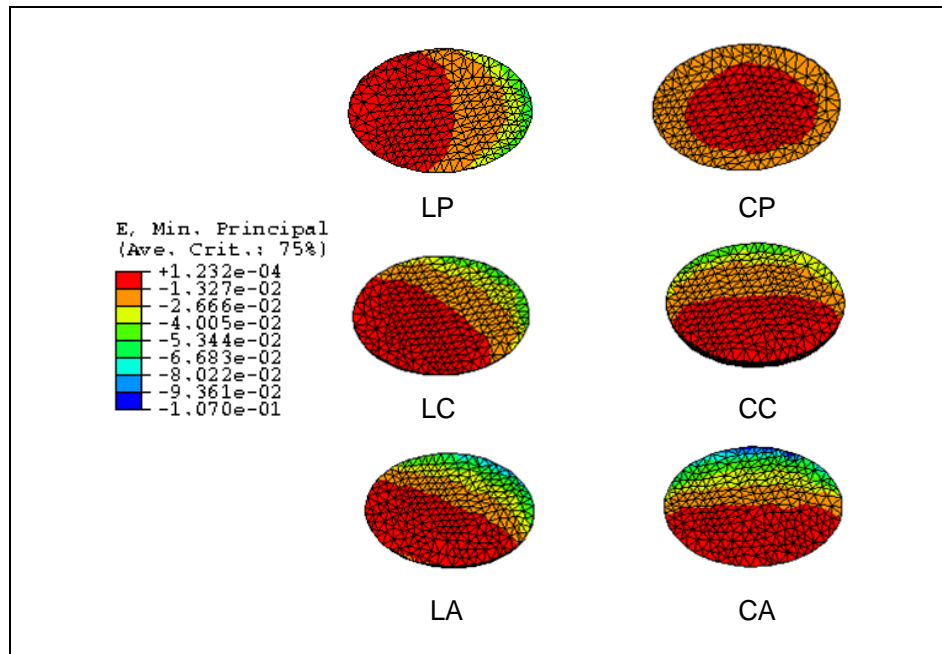


Figure 4.4: Contour plots of fusion mass for each location at a density of 0.15 g/cc showing strain distribution.

Strain distribution was also examined in the fused motion segment (Fig 4.5). Higher strains were seen along the peripheral edges of the fusion mass and within the vertebral body. However, no strain or stress concentrations were seen at the corners of the implant and vertebra.

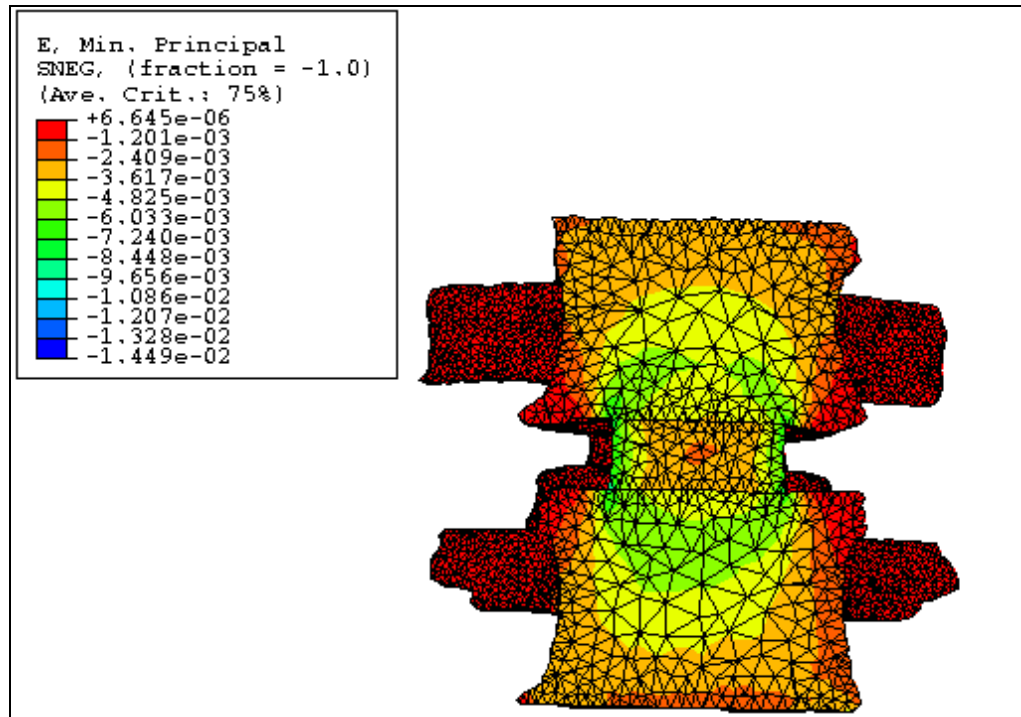


Figure 4.5: Contour plots of fused motion segment for a central-posterior location at a density of 0.30 g/cc showing strain distribution.

There are several notable strengths of this study. At present, there is little research that investigates the combined affects of fusion mass density and fusion mass location on the strength of the interbody fusion. This model not only considered these parameters but did so in a manner consistent with present day surgical techniques in order to increase the clinical applicability of the results. Other strengths

of this study include the anisotropic properties used to model the motion segment and results generated using a principal strain yield criterion (Morgan and Keaveny 2001).

Despite the strengths of this study, some limitations must be considered. Contact in the facet joints was neglected to show a worst-case scenario. Clinically, facetectomies and laminectomies are common procedures that accompany PLIF and TLIF procedures. Therefore, the lack of contact in the facet joints models a double facetectomy. If contact were modeled in the facet joints, some of the load would be distributed to the posterior elements, increasing the failure load. This would be most beneficial to the anterior and lateral locations in which the strain distribution was non-uniform. Because the exact composition of the allograft or autograft used in a fusion is usually unknown, this model used the failure strain of vertebral cancellous bone, 0.77%, (Morgan and Keaveny 2001) when calculating the failure strain for the entire model even though for lesser densities failure occurred in the fusion mass. This may have had some effect on the numerical values reported for the sustainable load and could be considered a limitation of the model. However, the observed trends will likely remain the same. Furthermore, the maximum load will differ from case to case as each patient will have varying characteristics that are important factors in this study such as vertebral body density, size of vertebral body, strength of vertebral body, and material properties of the fusion mass. The type of loading used in this model can also be considered a limitation. A compressive uniaxial pressure load was applied to the superior endplate of the superior vertebral body. However, other loading scenarios were neglected such as flexion and extension and lateral bending.

Although anisotropic properties are important for modeling bone accurately, the effects are negligible for this particular study. Because the loading was axial and along the principal direction of stress, similar results would be expected for the same model with isotropic properties. In fact, for a centrally placed fusion mass of 0.15 g/cc density, the maximum strain value differed by only 1.1% for the isotropic and anisotropic model. However, for future models with different loading scenarios such as flexion-extension or lateral bending, the anisotropic properties will be more important.

Correlations between our results and results obtained from other finite element analyses involving lumbar interbody fusion exist. Zander et al. showed that the influence of the elastic modulus of the bone graft was considerable regarding contact pressure and stress distribution. As the bone graft increased in stiffness, so did the maximum contact pressure (Zander, Rohlmann et al. 2002b). Similarly, in our study, for the highest fusion mass densities investigated, we saw evidence of subsidence indicative of greater contact pressure and increased stress on the endplate. Although our study, investigated compressive loading as opposed to flexion and lateral bending modeled by Zander, they also showed that stiffer grafts can increase the sustainable load. This was demonstrated experimentally by Jost et al. when investigating the compressive strength of interbody cages in the lumbar spine (Jost, Cripton et al. 1998). Adam et al. also demonstrated the clinical relevance of investigating interbody fusion systems during compressive loading showing that endplate subsidence failure can potentially occur at the corners of existing cage-type interbody implants under physiological compressive loads (Adam, Pearcy et al. 2003). These

studies, along with our results, show the utility of employing finite element analysis to investigate the various mechanical parameters involved in interbody fusion and show their clinical relevance.

CHAPTER 5

EFFECTS OF FACET JOINT CONTACT

5.1 Modeling Facet Joint Contact

The previously described models neglected contact between the facet joints. This idealizes a worst-case scenario and can be clinically compared to a double facetectomy. However, in minimally-invasive techniques, one or both facet joints may be spared. Facet joint contact allows for some of the load to be distributed through the posterior elements, and would, therefore, increase the maximum sustainable load until failure. The goal of this study was to investigate how contact in the facet joints affects the maximum load compared to a model that neglects contact.

5.2 Methods

Facet joint contact was directly defined in the Abaqus input file. The first step was to define node and element sets between the facet joints to designate as the master and slave surfaces. By choosing elements and nodes in Hypermesh, node and element sets were made to correspond to master and slave surfaces for each facet joint. Finite sliding was defined to allow for arbitrary motion between the two surfaces. Friction had to be added into the model as part of a surface interaction definition. A small friction coefficient of 0.02 was used typical of a synovial joint (Wright 1986).

The model originally had a gap between the facet joints where cartilage would be found because cartilage is nearly radio-lucent and was not visible on the CT scan. This had to be taken into account. This can increase the time of convergence or even cause the model to crash, never reaching a converged state. By defining an *hcrit* value in the Abaqus input file, these problems were addressed. However, after trying numerous values, the model failed to converge having severe discontinuity. Using this method combined with a decreased initial step size, the model converged to equilibrium.

The contact parameters that were identified were then applied to 24 different models, representing six fusion mass locations with four different fusion mass densities at each location. Similar to previous models, the Abaqus post-processor to obtain the maximum principal strain in the model as well as the total reaction force. Using these values along with the compressive failure strain of vertebral cancellous bone (0.77%) (Morgan and Keaveny 2001) in either the fusion mass or the vertebral body, the maximum sustainable load until failure was computed for each case using the following equation:

$$F_{Failure} = F_{Reaction} * \frac{\epsilon_{Failure}}{\epsilon_{Max}} \quad (1)$$

where $F_{failure}$ is the maximum sustainable load until failure, $F_{reaction}$ is the total reaction force in the model, $\epsilon_{failure}$ is the compressive failure strain of vertebral cancellous bone (0.0077), and ϵ_{max} is the maximum principal strain value. This equation assumes that the strains scale linearly with load. In the present case, the facet joint contact results in a non-linear relationship between loading and displacement, and, as such, the relationship needs to be further investigated. However, this formula

was used as a reasonable first approximation to the failure loads. The results were then examined to look for specific trends and to see how these results compared to the results obtained from the models that neglected contact in the facet joints.

5.3 Results

The same trends were seen for these new models as for those with no facet joint contact. As density increased, the failure load increased. As the fusion mass was posteriorly displaced, the failure load also increased. Lateral displacement resulted in a decreased failure load (Fig. 5.1).

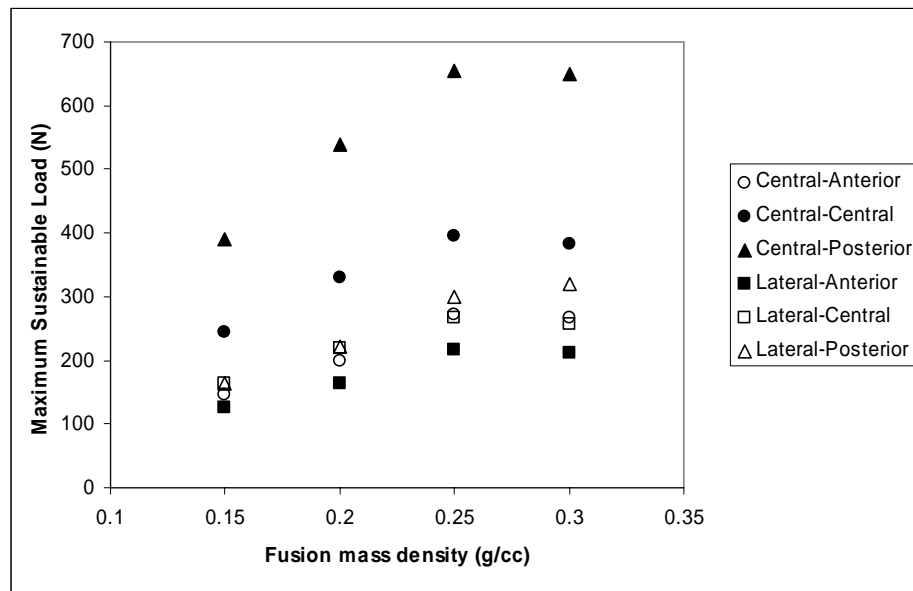


Figure 5.1: The maximum sustainable load (N) plotted for each fusion location as a function of fusion mass density (g/cc).

The results were compared to the results obtained from the previous chapter to examine the effects of contact in the facet joints have on the overall sustainable load.

The percent increase in load was calculated for each fusion location and fusion density (Figs. 4.2-4.5).

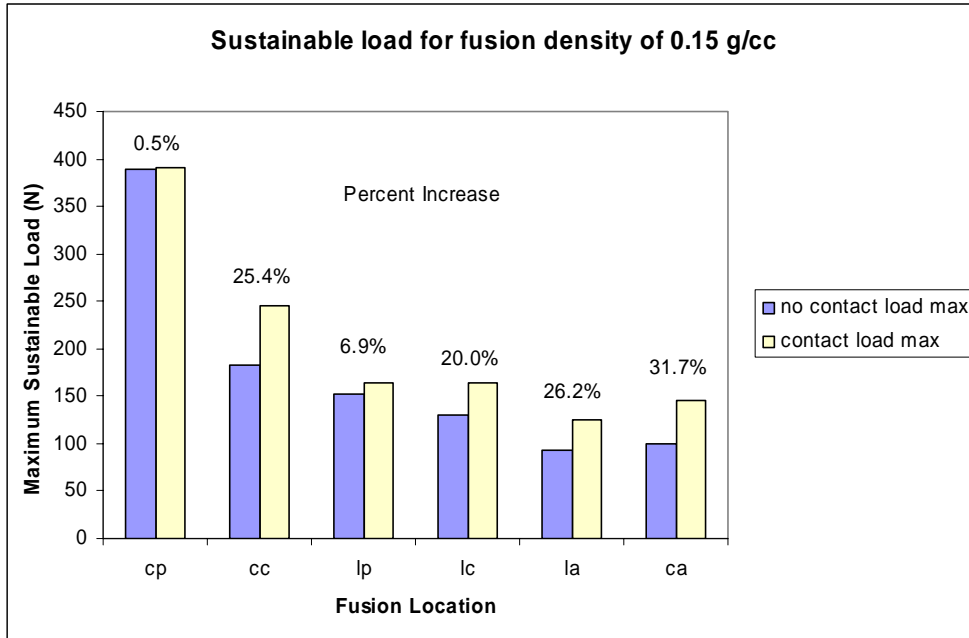


Figure 5.2: A comparison between the maximum sustainable load (N) with and without contact for a fusion mass density of 0.15 g/cc for each fusion location.

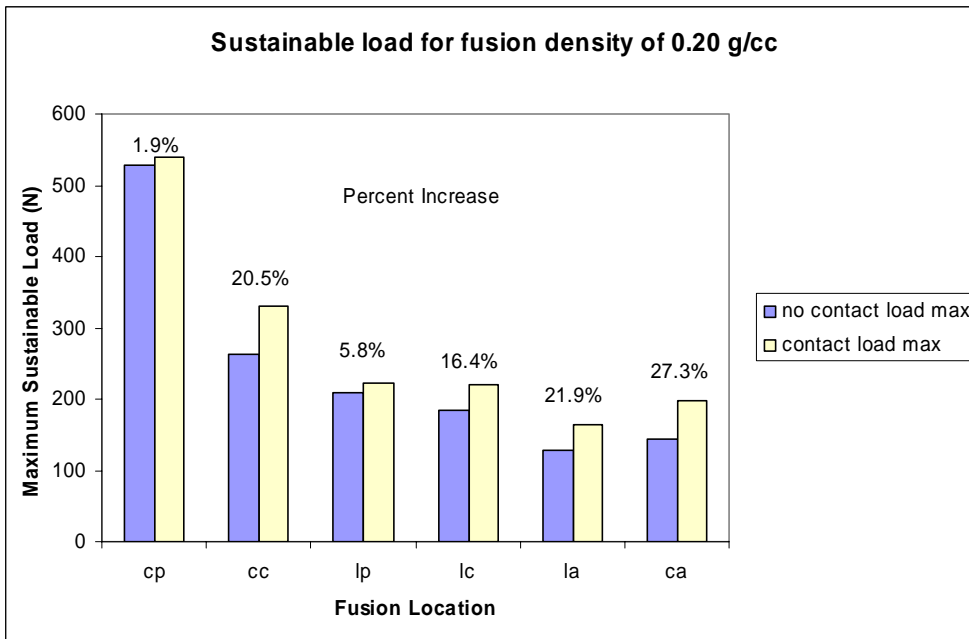


Figure 5.3: A comparison between the maximum sustainable load (N) with and without contact for a fusion mass density of 0.20 g/cc for each fusion location.

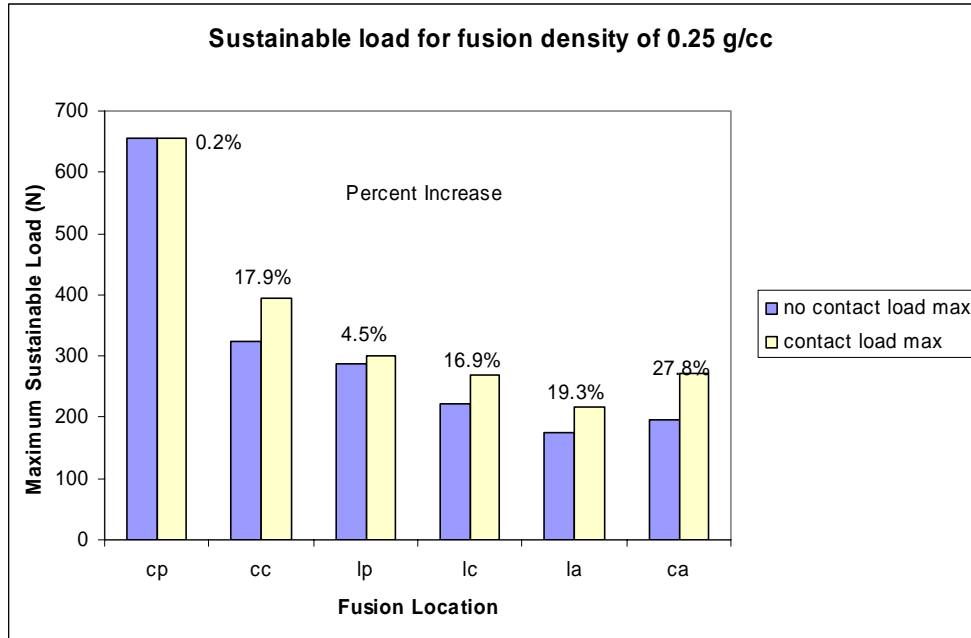


Figure 5.4: A comparison between the maximum sustainable load (N) with and without contact for a fusion mass density of 0.25 g/cc for each fusion location.

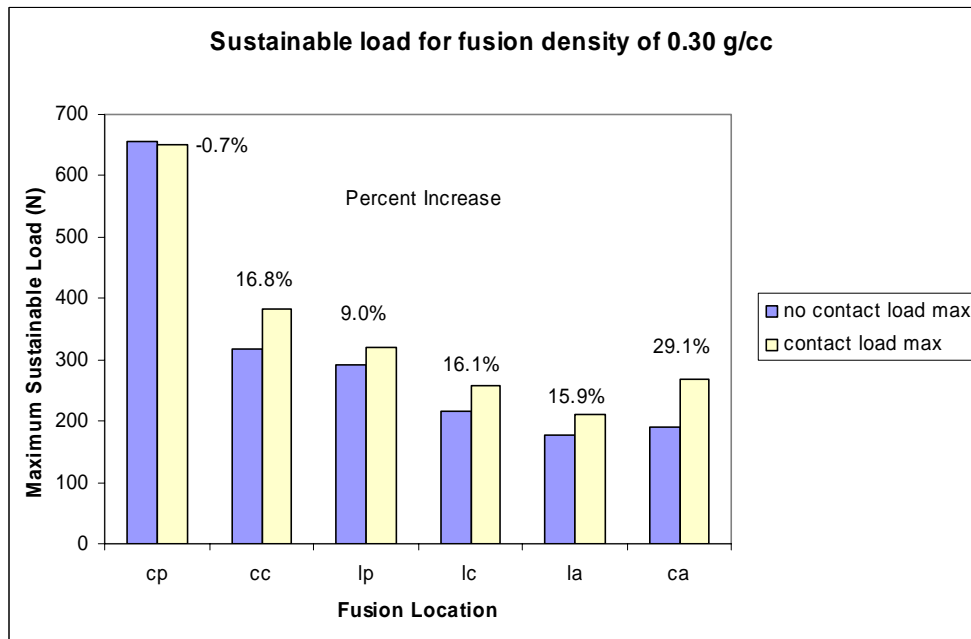


Figure 5.5: A comparison between the maximum sustainable load (N) with and without contact for a fusion mass density of 0.30 g/cc for each fusion location.

For the posterior fusion locations, contact had a negligible affect. This is especially true for the central-posterior position in which the maximum sustainable load until failure differed by at most 1.9% from the non-contact case. For the lateral-posterior fusion location, the greatest percent difference was seen when the fusion mass had a density of 0.30 g/cc. However, it was still relatively low at 9.0%. The greatest increase in the maximum sustainable load was consistently seen in the central-anterior position for all fusion densities with the greatest percent increase equal to 31.7% for a fusion mass density of 0.15 g/cc. For the other locations, central-central, lateral-central, and lateral-anterior, the maximum load was seen to increase between 15.9 and 26.2 percent for the different fusion densities.

Examining the results at different fusion mass densities, it is important to note, that although similar trends are seen for fusion location, the amount of load transferred to the facet joints is independent of the fusion mass density. The fusion mass density was negligible when comparing contact versus no contact in the facet joints.

5.4 Discussion

The goal of this study was to compare the effect contact in the facet joints has on the overall strength of an interbody fusion. The clinical relevance of this study is that it can be correlated to the effects of a double facetectomy. The results suggest that contact in the facet joints increases the stability in the interbody fusion allowing some of the load to be redistributed through the posterior elements increasing the maximum sustainable load. However, the increased sustainable load is fusion location

dependent. Zander et al. also showed decreased spinal stability after graded facetectomy using finite element analysis (Zander, Rohlmann et al. 2003). The posterior elements would be more likely to contribute to resisting loads caused by lateral bending or flexion-extension (Miller, Haderspeck et al. 1983).

There have been many conflicting publications about how much of the vertical load the facets are capable of carrying. According to Nachemson, it was concluded that through experimental study, the facets were capable of carrying approximately 20% of the axial load (Nachemson 1960). However, only three years after publishing these results, he retracted his previously made conclusions (Nachemson 1963). Later on, more experimental studies were performed to indicate that the facets do support a portion of the load. Adams et al. performed experimental compression tests of lumbar vertebrae to quantify that the facets are responsible for bearing 16% of the load seen in erect standing (Adams and Hutton 1980). These studies, measure the load transmitted to the facet joints with an intact disc. This percentage could change if the intervertebral disc is replaced with a fusion mass. Furthermore, the location of the fusion mass will affect how much of the load will be transmitted to the facet joints. Although the average percent increase in allowable load for all fusion locations and fusion densities was 15.78% and this is comparable to published experimental values, more research needs to be done to assess the validity of these results.

CHAPTER 6

CONCLUSION

6.1 Goal of this Study

The overall goal of this research was to investigate the effects of variations in the bone density and fusion mass location in lumbar interbody fusion. Specifically, the aims were to 1) develop a three dimensional finite element model of a lumbar motion segment, 2) analyze the effect of fusion mass location and density on the maximum load to failure, and 3) relate our findings to clinical application.

6.2 Summary

A preliminary model was created that investigated fusion mass density and fusion mass location. It showed that lateral displacement of the fusion mass significantly decreases the strength of a lumbar interbody fusion (LIF). This model also showed that as density increases the max load to failure increases.

A more detailed model was created to include anisotropy and the posterior elements. This model investigated density affects in the fusion mass including the effects of concentrically varying the density of the fusion mass. It showed that the strength of the LIF was dependent upon the density of the fusion mass. The strength of the LIF increased as the density of the fusion mass increased. However, when the fusion mass was comprised of varying densities, an inner region density and an outer

ring region density, the strength of the LIF was comparable to the strength seen with a fusion mass having a density equal to the density of the outer ring.

Parameter studies were performed to verify the performance of the model. The solutions were verified to be converged, and the sensitivity of the methods used to detect failure was investigated.

A detailed model was used to investigate the effects of fusion location in six different positions while varying the fusion mass density. This model showed that a central-posterior fusion location had the highest load to failure under compression. The same density affects were seen as in previous models, as density increased, maximum load to failure increased. However, this model incorporated higher densities to show that at a certain point, this relationship is no longer valid. Subsidence or graft settling will cause failure when the fusion mass becomes too dense.

The effects of contact in the facet joints were also researched. These results were compared to a model with no contact in the facet joints. The model with contact, on average, supported a 15.7% higher load. The increase in sustainable load was fusion location dependent. Contact in the facet joints was most beneficial to anterior and lateral fusion positions.

6.3 Future Work

In the future, this research could be supplemented in many ways. First of all, there is currently work being done investigating material properties of lumbar vertebral bone using the micro CT scanner. Multiple vertebral bodies will be scanned for statistical

relevance. An elastic modulus in the superior-inferior direction and transverse directions will be assigned for nine locations occurring in three different transverse planes. This will allow for increased accuracy in material property definition. These results will then be applied to the model.

Next, different loading conditions should be applied to this model to investigate the effects of lateral bending and flexion-extension movement. This would be important, because these loading scenarios will have different effects depending upon where the fusion mass is placed. Contact in the facet joints will also be important in regards to these loading conditions and will most likely take a more noticeable role. However, using these loading scenarios with or without contact in the facet joints requires us to further examine the relationship used to obtain the failure load in the previous models. This relationship:

$$F_{Failure} = F_{Reaction} * \frac{\epsilon_{Failure}}{\epsilon_{Max}} \quad (1)$$

where $F_{failure}$ is the maximum sustainable load until failure, $F_{reaction}$ is the total reaction force in the model, $\epsilon_{failure}$ is the compressive failure strain of vertebral cancellous bone (0.0077) (Morgan and Keaveny 2001), and ϵ_{max} is the maximum strain value is based on a linear elastic relationship. When the models are linearly elastic, this relation effectively scales the load to the level that would result in the minimum principal strain exceeding the failure strain. Studies show that when expressed in terms of strain, failure criteria for a given site may consider the yield point constant for uniaxial monotonic loading (Morgan and Keaveny 2001). A failure criteria involving Von Mises stress is a possible option.

Another future endeavor is to do an analysis on fusion mass size in relation to the previous studies. Currently, the models use a fusion mass that covers approximately 33% of the area of the vertebral body endplate (Closkey, Parsons et al. 1993). Since the central-central and posterior-central fusion location were the strongest under the compressive loading, it would be interesting to research the size of the fusion mass needed at the other locations, specifically the anterior locations, to achieve the same strength.

Adding hardware is another possibility for the future. Exact geometries could be obtained for screws or rods used in interbody fusion procedures. The hardware could then be added to the model. This would create a stabilizing effect for the motion segment; however, it would induce stresses in the posterior elements where the screws and rods are usually placed. This may require additional consideration of these stresses.

6.4 Conclusions

Many conclusions can be drawn from the research presented in this thesis. Most importantly, specific inferences were made regarding the effects of fusion mass density and fusion mass location on the maximum sustainable load to failure. These conclusions are summarized below:

- As the fusion mass density is increased, the strength of the lumbar interbody fusion (LIF) increases. Increasing the density past a certain point where the fusion mass is as dense or more dense than that of the vertebral body will not increase the strength of the LIF but will most likely result in subsidence.
- A fusion mass with a denser outer ring and less dense inner core demonstrated a LIF strength almost equivalent to having a fusion mass

entirely of the denser substance. A fusion mass with a less dense outer ring and a more dense inner core demonstrated a LIF strength almost equivalent to having a fusion mass entirely of the less dense substance.

- As the fusion mass is displaced laterally, the strength of the lumbar interbody fusion decreases. As the fusion mass is displaced anteriorly, the strength of the lumbar interbody fusion decreases. A posteriorly placed fusion mass has a more uniform strain distribution under compressive loading allowing for the LIF to carry more load.
- The same trends in regards to fusion mass density and fusion mass location are seen when modeling contact and no contact in the facet joints.
- Contact in the facet joints was most beneficial to the non-posterior fusion locations. For the posterior fusion locations, contact had a negligible affect.

APPENDIX A1

PROCEDURE FOR CREATING A TRIANGULATED SURFACE MESH

ORTHOPAEDIC TISSUE MECHANICS LAB
Department of Aerospace and Mechanical Engineering
University of Notre Dame

TITLE: Transformation of CT images to a Triangulated Surface Mesh of a Lumbar Motion Segment

A. OBJECTIVE

Obtain a 3D triangulated surface mesh of a lumbar motion segment.

B. MATERIALS

(1) Cross-sectional CT images of lumbar spine

C. TOOLS

- (1) computer
- (2) NIH Image
- (3) IDL
- (4) Polyr
- (5) IVVIEW

D. PROCEDURE

Note: *It is easiest to work with tiff images in IDL.*

Upload dicom images into NIH and resave them as tiff images. To correspond with IDL the following format is advised how each image should be saved: *prefix.#####.tif*. For example, *image.0123.tif* is an appropriate file name.

Because the images are cross-sectional slices spaced XX mm apart, the data between each slice needs to be interpolated. The following steps outline this procedure:

Procedure 1:

- (1) Open IDL by typing *IDL* in the Unix command window.
- (2) To load the tiff images, type:
images=tiff_load()
where *images* is a user specified variable.
- (3) This then prompts the user for the following information:
Specimen directory: enter directory where images are saved
Specimen suffix: enter file extension, i.e., *tif*
Enter first slice: enter starting slice #
Enter slices to read: enter total number of images to be read
Filename prefix: enter the filename prefix
3 or 4 digits: enter 1 for 3 digits and 2 for four digits
- (4) The next command:
images2=255b-images
will invert the image where *images2* is a user specified variable. **Note:** This may not be necessary.
- (5) Before interpolating the missing data between the slices, the new dimensions need to be determined. This is calculated using the following
$$\text{number of pixels/mm} * \text{mm/slice} * \text{number of slices} = 512/134 * 1.5 * 143 = 819$$
- (6) The *congrid* command allows for the interpolation of data between the slices. It is set up as:
result=congrid(Array,X,Y,Z[, cubic=value{-1 to 0}][interp][,/minus_one])
where *result* is a user specified variable. *Array* refers to the three dimensional array that needs to be resized and requires the input of the resized x, y, and z dimensions. For example, the code should resemble this: *imagenew=congrid(image2,512,512,819,cubic=-0.5)*.
- (7) The new images need to be resaved as tiff images to work with in NIH Image. The command format to use is:
save_as_tiff, file name, 'new file name'.
For example:
save_as_tiff,imagenew,'new_image.512.512.819.'
is appropriate format. **Note:** It is good to save the file with the dimensions in the prefix to refer to later. Also, you do not need to add

the file extension, i.e., tiff. If the dimensions are unknown, *help,array* outputs the dimensions of an array.

From this point, the images can be opened in NIH Image and various thresholding techniques can be applied to get the desired black and white image. The following exemplifies this process:

Procedure 2:

- (1) Under *file*, select *import* to upload images. **Note:** The number of images that can be uploaded at one time is memory dependent.
- (2) Using the pencil tool, one pixel wide lines were drawn to outline the desired region of the vertebral body to include posterior elements and exclude such abnormalities as osteophytes.
- (3) The “bone” material of the image was set white using the eyedropper tool.
- (4) Under the *options* menu, enabling the *threshold* allows to remove all gray areas in the image, displaying a black and white image.
- (5) The image is then resaved, overwriting the previous image at the user’s discretion.

The next procedure explains the how to form the triangulated surface mesh:

Procedure 3:

- (1) The images are then reread into IDL using Procedure 1 steps 1-3. The image may need to be inverted using Procedure 1 step 4 if the white portion of the image was read in as black and the black portion of the image was read in as white. In order to view the model to see if this is necessary, the command, *render*, is useful. By typing *render, image*, where *image* is the user-defined variable used in the previous steps, IDL render the image.
- (2) In order to soften the edges of the created volume, the smooth function should be used. The *smooth* function returns a copy of an array that is smoothed with a boxcar average of a user specified width. For example:
result=smooth(array,width)
where *result* is a user specified variable. The width should be an odd number and refers to the number of elements in each direction. For example, a width of 3 for a three-dimensional array would have a smoothing window that contained 27 elements.
- (3) In order to view the volume, the command *render* can be used to view it. For example:
render,image
allows you to view the 3-D volume given the variable name, *image*. This allows the user to visualize if the volume needs to be smoothed more.
- (4) The image then needs to be written to a binary file using the *write_bindat,'filename.by',variable* command. Similar to writing images to tiff files, it is advisable to save the binary file under a file name that contains the dimensions of the three-dimensional array. For example:

write_bindat, 'image.x.y.z.by' ,image

where x, y, and z would represent the numerical dimension of the array in that particular direction.

(5) Type *exit* to exit idl.

(6) The program *polyr* creates the triangulated surface mesh in the form of a .iv file. The command format is as follows:

polyr -i filename -r # of triangles -raw x-dim y-dim z-dim file.by threshold.

The following exemplifies this:

polyr -i vrtbrlbody1 -r 100000 398 446 129 vrtbody1.398.446.129.by 250 .

This would create the file *vrtbrlbody1.iv* as well as outputting the number of triangles used to create the surface. Depending, on the complexity of the geometry, it is not uncommon to have a surface consisting of over 1,000,000 triangles. At this point, it would be advisable to reduce the number of triangles in the command line.

(7) The program *IVVIEW* allows you to view the triangulated surface by simply typing *ivview* and the file name:

ivview vrtbrlbody1.iv.

Viewing the surface can also help to decide how many triangles should be used in the surface mesh. If there is not enough detail present, more triangles should be used. If the surface needs to be smoothed, fewer triangles should be used.

APPENDIX A2

PROCEDURE FOR CREATING A FINTE ELEMENT MESH

ORTHOPAEDIC TISSUE MECHANICS LAB
Department of Aerospace and Mechanical Engineering
University of Notre Dame

TITLE: Guidelines for Creating a Finite Element Mesh from a Triangulated Surface Mesh

A. OBJECTIVE

Obtain a 3D finite element mesh from a triangulated surface mesh.

B. MATERIALS

(1) Triangulated surface mesh

C. TOOLS

- (1) Computer (SGI)
- (2) IVREAD
- (3) Finite element meshing program

D. PROCEDURE

Note: The following procedure is most specific to the finite element program, Hypermesh.

- (1) An appropriate file format is needed to import a triangulated surface mesh into a finite element meshing program. Usually, an *.stl* (ASCII Stereolithography) file is compatible with most finite element meshing programs. Make sure to see if this is true with the chosen meshing program.
- (2) The program, IVREAD, is valuable for converting a 3D triangulated surface mesh into an *stl* file. Many file formats can be used with this program. For example, if the triangulated surface mesh is a *.iv* (SGI inventor) file the following command will convert the file to an *.stl* file:
ivread input.iv output.stl
- (3) An *.stl* file is readily importable into Hypermesh. Under the files tab, select *import* from the sub-menu on the left. Enter the file name along with the appropriate directory, check the *STL* box and press the *import* button.
- (4) A surface mesh is automatically created in the viewing window.

WORKS CITED

- Adam, C., M. Pearcy, et al. (2003). "Stress analysis of interbody fusion--finite element modelling of intervertebral implant and vertebral body." Clin Biomech (Bristol, Avon) **18**(4): 265-72.
- Adams, M. A. and W. C. Hutton (1980). "The effect of posture on the role of the apophysial joints in resisting intervertebral compressive forces." J Bone Joint Surg Br **62**(3): 358-62.
- Belytschko, T., R. F. Kulak, et al. (1974). "Finite element stress analysis of an intervertebral disc." J Biomech **7**(3): 277-85.
- Closkey, R. F., J. R. Parsons, et al. (1993). "Mechanics of interbody spinal fusion. Analysis of critical bone graft area." Spine **18**(8): 1011-5.
- Crawford, R. P., W. S. Rosenberg, et al. (2003a). "Voxel-based finite element models of the human thoracolumbar vertebral body: effect of element size on stiffness, damage, and fracture strength predictions." Journal of Biomechanical Engineering (in press).
- Crawford, R. P., W. S. Rosenberg, et al. (2003b). "Quantitative computed tomography-based finite element models of the human lumbar vertebral body: effect of element size on stiffness, damage, and fracture strength predictions." J Biomech Eng **125**(4): 434-8.
- DeBowes, R. M., B. D. Grant, et al. (1984). "Cervical vertebral interbody fusion in the horse: a comparative study of bovine xenografts and autografts supported by stainless steel baskets." Am J Vet Res **45**(1): 191-9.
- Goel, V. K. and L. G. Gilbertson (1995a). "Applications of the finite element method to thoracolumbar spinal research--past, present, and future." Spine **20**(15): 1719-27.
- Goel, V. K., S. A. Ramirez, et al. (1995b). "Cancellous bone Young's modulus variation within the vertebral body of a ligamentous lumbar spine--application of bone adaptive remodeling concepts." J Biomech Eng **117**(3): 266-71.
- Heary, R. F. and C. M. Bono (2002). "Circumferential fusion for spondylolisthesis in the lumbar spine." Neurosurg Focus **13**.

- Jost, B., P. A. Cripton, et al. (1998). "Compressive strength of interbody cages in the lumbar spine: the effect of cage shape, posterior instrumentation and bone density." Eur Spine J **7**(2): 132-41.
- Katz, J. N. (1995). "Lumbar spinal fusion. Surgical rates, costs, and complications." Spine **20**(24 Suppl): 78S-83S.
- Kawaguchi, Y., H. Matsui, et al. (1998). "Preventive measures of back muscle injury after posterior lumbar spine surgery in rats." Spine **23**(21): 2282-7; discussion 2288.
- Keaveny, T. M., E. F. Morgan, et al. (2001). "Biomechanics of trabecular bone." Annu Rev Biomed Eng **3**: 307-33.
- Kong, W. Z., V. K. Goel, et al. (1998). "Prediction of biomechanical parameters in the lumbar spine during static sagittal plane lifting." J Biomech Eng **120**(2): 273-80.
- Kumar, A., J. A. Kozak, et al. (1993). "Interspace distraction and graft subsidence after anterior lumbar fusion with femoral strut allograft." Spine **18**(16): 2393-400.
- Liebschner, M. A., D. L. Kopperdahl, et al. (2003). "Finite element modeling of the human thoracolumbar spine." Spine **28**(6): 559-65.
- Miller, J. A., K. A. Haderspeck, et al. (1983). "Posterior element loads in lumbar motion segments." Spine **8**(3): 331-7.
- Morgan, E. F., H. H. Bayraktar, et al. (2003). "Trabecular bone modulus-density relationships depend on anatomic site." J Biomech **36**(7): 897-904.
- Morgan, E. F. and T. M. Keaveny (2001). "Dependence of yield strain of human trabecular bone on anatomic site." J Biomech **34**(5): 569-77.
- Nachemson, A. (1960). "Lumbar intradiscal pressure. Experimental studies on post-mortem material." Acta Orthop Scand Suppl **43**: 1-104.
- Nachemson, A. (1963). "The Influence of Spinal Movements on the Lumbar Intradiscal Pressure and on the Tensile Stresses in the Annulus Fibrosus." Acta Orthop Scand **33**: 183-207.
- Nachemson, A. L. (1992). "Newest knowledge of low back pain. A critical look." Clin Orthop(279): 8-20.
- Nicholson, P. H., X. G. Cheng, et al. (1997). "Structural and material mechanical properties of human vertebral cancellous bone." Med Eng Phys **19**(8): 729-37.

- Panjabi, M. M., V. Goel, et al. (1992). "Human lumbar vertebrae. Quantitative three-dimensional anatomy." Spine **17**(3): 299-306.
- Pokras, R. and K. K. Kubishke (1985). "Diagnosis-related groups using data from the National Hospital Discharge Survey: United States, 1982." Adv Data(105): 1-8.
- Ray, C. D. (1997). "Threaded titanium cages for lumbar interbody fusions." Spine **22**(6): 667-79; discussion 679-80.
- Sandhu, H. S., S. Turner, et al. (1996). "Distractive properties of a threaded interbody fusion device. An in vivo model." Spine **21**(10): 1201-10.
- Silva, M. J., C. Wang, et al. (1994). "Direct and computed tomography thickness measurements of the human, lumbar vertebral shell and endplate." Bone **15**(4): 409-14.
- Smit, T. H., A. Odgaard, et al. (1997). "Structure and function of vertebral trabecular bone." Spine **22**(24): 2823-33.
- Ulrich, D., B. van Rietbergen, et al. (1999). "The ability of three-dimensional structural indices to reflect mechanical aspects of trabecular bone." Bone **25**(1): 55-60.
- Weiner, B. K. and R. D. Fraser (1998). "Spine update lumbar interbody cages." Spine **23**(5): 634-40.
- Whitecloud, T. S., 3rd, W. W. Roesch, et al. (2001). "Transforaminal interbody fusion versus anterior-posterior interbody fusion of the lumbar spine: a financial analysis." J Spinal Disord **14**(2): 100-3.
- Whyne, C. M., S. S. Hu, et al. (1998). "Effect of the pedicle and posterior arch on vertebral body strength predictions in finite element modeling." Spine **23**(8): 899-907.
- Wolff, J. (1892). Das Gesetz der Transformation der Knochen. Translated as: The Law of Bone Remodelling. Springer, Berlin.
- Wright, V. (1986). "Heberden oration 1985. The rheology of joints." Br J Rheumatol **25**(3): 243-52.
- Zander, T., A. Rohlmann, et al. (2002a). "Comparison of the mechanical behavior of the lumbar spine following mono- and bisegmental stabilization." Clin Biomech (Bristol, Avon) **17**(6): 439-45.

Zander, T., A. Rohlmann, et al. (2002b). "Effect of bone graft characteristics on the mechanical behavior of the lumbar spine." J Biomech **35**(4): 491-7.

Zander, T., A. Rohlmann, et al. (2003). "Influence of graded facetectomy and laminectomy on spinal biomechanics." Eur Spine J **12**(4): 427-34.